Automated Segmentation of Lung Nodules and Pulmonary Blood Vessels and Follow-up Analysis of Lung Nodules from 3D CT Images

Bin Chen

Acknowledgements

I would like to express my warm and most sincere gratitude to my honorable supervisor, Prof. Dr. Kensuka Mori, who made my dissertation possible. Without his guidance, encouragement, and support, I could have never finished my doctoral work. He has been an excellent advisor and has always directed me in doing my fundamental research that will make a difference. Moreover, his broad knowledge in computer-aided detection/diagnosis, meticulous attitude in academic research, and excellent experience in medical image analysis has been of major help to me and we have had many fascinating discussions on a large variety of topics.

I woud also like to convey my heartfelt thanks to Prof. Dr. Hiroshi Murase for his help during my doctoral study, as well as the insightful suggestions he gave me in regards to my research before starting my thesis and his willingness to be my thesis reviewer. I am also very grateful to Prof. Dr. Noboru Ohnishi and Associate Prof. Dr. Shigeki Matsubara who gave me precious comments and were also willing to review my thesis and are deserving of my sincere thanks. My warm thanks is also due to Associate Prof. Dr. Yoshinori Takeuchi for his advice on my work.

I owe my sincere gratitude to Dr. Hiroshi Honma (Sapporo Medical University), Dr. Hirotsugu Takabatake (Sapporo Minami-Sanjo Hospital), Dr. Masaki Mori (Sapporo-Kosei general Hospital), and Dr. Hiroshi Natori (Keiwakai Nishioka Hospital) for their helpful medical advice, and their valuable materials.

I am heartily deeply grateful to Prof. Dr. Takayuki Kitasaka (Aichi Institute of Technology) for his suggestions and discussions in regard to my study since 2007. His knowledge and experience regarding my work were a great assistance to resolve my various doubts in regards to my dissertation. Much thanks is also due to Prof. Dr. Yasuhito Suenaga (Aichi Institute of Technology) for his warm encouragement during his

time at Nagoya University from 2007 to 2009. His encouragement and help made me feel confident to fulfill my desire and to surmount the numerous difficulties associated with my study. I would also like to express my gratitude to Prof. Dr. Yoshito Mekada (Chukyo University) for his generous supports on my study.

I am deeply grateful to my seniors at Mori laboratory: Dr. Masahiro Oda, Dr. Yukitaka Nimura, Dr. Yuichiro Hayashi, Dr. Xiongbiao Luo, Dr. Zhengang Jiang and Dr. Yoshihiko Nakamura for their insightful comments and suggestions in regard to my study since 2007. I would also like to thank all my colleagues at Mori laboratory for their useful discussions in regards to my doctoral research. Special thanks to the secretary of Mori laboratory, Rie Ohashi for her great clerical work and her assistance with my business trips.

I owe a great deal to all the organizations, who generously sponsored my study, including the NGK Foundation for International Students, the Hattori Kaigai Ryugakusei Ikueikai, the Morita Scholarship Foundation and Ban-bun-Tane Houtoku-Kai Foundation. Without their support and financial help, it would not have been possible for me to complete my doctoral thesis successfully.

I would also like to express my great appreciation to my uncle Jianguo Wang and aunt Xiaojuan Fang, who have fully supported me since the beginning of my study in Nagoya.

Finally I would like to extend my indebtedness to my parents, Xinlong Chen and Jianying Wang for their endless love, understanding, support, encouragement and sacrifice throughout my study.

Contents

Contents **i**

List of Figures **vii**

List of Tables **xiii**

1 Introduction **1**

1.1 Lung Anatomy 2

1.2 Lung cancer 3

1.2.1 Overview 3

1.2.2 Types of lung cancer 4

1.2.3 Diagnosis of lung cancer 4

1.2.4 Treatment of lung cancer 5

1.3 Lung nodule 6

1.3.1 What is lung nodule? 6

1.3.2 Relation between lung nodule and lung cancer 6

1.3.3 Types and shapes of lung nodules 7

1.4 Computer Tomography (CT) 7

1.4.1 History of CT 7

1.4.2 Lungs on CT 8

1.4.3 Lung nodules on CT 9

1.4.4 Role of CT in the diagnosis and treatment of lung cancer (lung nodule) 10

1.4.5 Benefits and problems 11
1.5 CAD system 12
1.5.1 Overview 12
1.5.2 General framework of CAD 13
1.5.3 Current status of CAD 14
1.5.3.1 Breast CAD system on mammogram 14
1.5.3.2 Colon CAD system on CTC 15
1.5.3.3 Chest CAD system 16
1.6 Organization of this thesis 17

2 Technique and related work of chest CAD system 19
2.1 General techniques 19
2.1.1 Medical image segmentation 19
2.1.2 Classification 21
2.1.3 Registration 21
2.2 Purpose of our research 22
2.3 Related work 23
2.3.1 Lung nodule segmentation 24
2.3.1.1 Nodule candidate detection method 24
2.3.1.2 False positive (FP) reduction 26
2.3.2 Pulmonary vessel segmentation 27
2.3.3 Lung nodule matching 27
2.4 Disadvantages of previous methods 30
2.5 Basic ideas in this dissertation 31
2.6 Main contributions 33
2.6.1 New approaches 33

3 Automated segmentations of lung nodules and pulmonary blood vessels from 3D chest CT images 35
3.1 Purpose 35

3.2 Methods . . . 38
3.2.1 Overview . . . 38
3.2.2 Preprocessing . . . 40
3.2.3 Local intensity structures analysis . . . 41
3.2.4 Fine segmentation of pulmonary blood vessel and nodules . . . 46
3.2.4.1 Front surface propagation (FSP) . . . 46
3.2.4.2 Initialization of front surface . . . 47
3.2.4.3 Construction of speed function . . . 48
3.2.4.4 Correction of front surface . . . 49
3.2.4.5 Final segmentation . . . 52
3.3 Experiments . . . 52
3.4 Results . . . 57
3.4.1 Validation of pulmonary blood vessel segmentation . . . 57
3.4.2 Validation of pulmonary nodule segmentation . . . 59
3.4.3 Comparison with conventional methods . . . 63
3.5 Discussion . . . 64
3.5.1 Effectiveness of optimum surface fitting . . . 64
3.5.2 Effectiveness of fine segmentation for pulmonary blood vessel segmentation . . . 65
3.5.3 Effectiveness of fine segmentation for pulmonary nodule detection . . . 67
3.5.4 Limitations . . . 68
3.6 Conclusion . . . 70

4 Automated matching of lung nodules on follow-up CT scans 71
4.1 Purpose . . . 71
4.2 Methods . . . 73
4.2.1 Overview . . . 73

4.2.2 Preprocessing . . . 74
4.2.3 Registration of CT images . . . 75
4.2.4 Similarity calculation of nodules . . . 76
4.2.4.1 Similarity measure . . . 76
4.2.4.2 Similarity calculation patterns . . . 78
4.2.4.3 Constraints of similarity calculations . . . 82
4.2.5 Corresponding nodule finding . . . 86
4.3 Experiment and results . . . 86
4.3.1 Materials and parameter estimation . . . 86
4.3.2 Comparison with previous methods . . . 91
4.4 Discussion . . . 91
4.4.1 Effectiveness of proposed method on reducing false matching . . . 91
4.4.2 Effectiveness of the similarity calculation of $Pattern\ 2$ . . . 92
4.4.3 Effectiveness of $Constraint\ 3$ . . . 93
4.4.4 Limitations . . . 95
4.5 Conclusions . . . 96

5 Conclusions and future work **97**
5.1 Summary . . . 97
5.2 Benefits and limitations . . . 99
5.2.1 Benefits . . . 99
5.2.2 Potential limitations . . . 100
5.2.2.1 Limitations of segmentations . . . 100
5.2.2.2 Limitations of nodule matching . . . 100
5.3 Future work . . . 101
5.3.1 Improvement of proposed methods . . . 101
5.3.2 Further development of chest CAD system . . . 102
5.3.3 Other applications . . . 104

Bibliography **107**

Publications **129**

List of Figures

1.1 Illustration of lung anatomy in 2D. 2

1.2 Three separated axial sections of a 3D CT volume. (a) shows an example of an axial section, (b) shows an example of a sagittal section, and (3) shows an example of a coronal section of one CT volume. 9

1.3 Illustrations of lung nodules on CT image. (a) shows a well-circumscribed nodule, (b) shows two vascularized nodules, (c) shows a pleural tail type, and (d) shows a juxtapleural nodule. 10

1.4 Illustration of the general framework of the CAD system. 13

2.1 The illustration of the developing chest CAD system. A chest CT database is constructed to storage the follow-up CT images of all the patients. All of the CT images in the database are processed by the segmentation of nodules and organs, and the automated matching of segmented nodules. When a new CT image of one patient is generated, the automated segmentation of nodules and organs will be executed on it. Then, automated nodule matching between the current CT image and the last CT image in the database is performed, and the report of nodule growth can be obtained from the matching results. By analyzing the nodule growth and other information recorded in the database, the system can give several suggestions for the treatment, metastatic situation and therapy planning. 23

2.2 Illustration of the basic ideas and the disadvantages of previous methods to be solved in this dissertation. 32

3.1 The problems in the nodule matching and the solutions of the proposed method 36

3.2 Volume rendering of a chest CT image. There are hundreds of lung nodules generated in the lungs of this patient. We mark the different nodules with different colors. The nodules pointed with white narrows are the vessel-attached ones. To separate such nodules from blood vessels is difficult. 37

3.3 Examples of a vessel-attached nodule and blood vessel bifurcation point. 37

3.4 Flowchart of the proposed method 39

3.5 Extraction of a processing target region I_{target}. (a) shows an axial slice of a chest CT image. (b) shows the segmentation results of the target processing region I_{target} (blue regions). 40

3.6 Eigenvalue distribution of the Hessian matrix during local intensity structure analysis [145]. (a) shows eigenvalues of the Hessian matrix on a branch of blood vessels, (b) shows eigenvalues of a Hessian matrix on a nodule and (c) shows eigenvalues on a vessel bifurcation. 42

3.7 Results of line structure enhancement filters. (a) The volume of the original synthetic image (b) One slice of the original synthetic images, (c) The result of previous LSE filter [111] and (d) The result of the newly proposed LSE filter. 44

3.8 Segmentation of initial front surface I_{hilar}. (a) shows an axial slice of a chest CT image that contains a carina. The starting point of the region growing is the centerline point of ascending aorta, (b) shows the segmentation results of region I_1, (c) shows region I_2 and (d) shows region I_{thick} utilized as the initial front surface. 47

3.9 Illustration of *nodule checking processing*. Front surface that terminates at blood vessel regions usually shows an irregular shape (A(i) in Fig. 3.9), whereas the one terminated at nodules shows a regular spherical shape (B(i) in Fig. 3.9). During *nodule checking processing*, we first select whole front surfaces S_i that stopped at nodule candidates (A(ii) and B(ii) in Fig. 3.9).Volume region of B_i is extracted using region growing from S_i, and the centroid G of B_i is found (A(iii) and B(iii) in Fig. 3.9). Add each B_i that is considered a non-nodule into front surface (Fig. 3.9(A(v)). For that considered a nodule, restore the nodule candidates that correspond to B_i (B(v) in Fig. 3.9). 51

3.10 Average response of MS_LSE and MS_BSE filters. Blue curves show the average response without normalization on single scale arranged 1.0 mm to 8.0 mm with step of $1.0\ mm$, and red ones show the curve by normalization. Normalization factor γ of MS_LSE and MS_BSE filters is r_i^2 and $r_i^{3/2}$, respectively. 54

3.11 Illustration of normalized responses of LSE and BSE filters on different scales (the radius of local region) at the center of different structures in Fig. 3.7. The largest responses of both BSE and LSE filters are obtained when the scale is approximate to the radius of objective structures. (a) shows the responses of LSE filter at line structures with different radii $(1.25, 2.5, 5, 10mm)$, and (b) shows the responses of the BSE filter at blob structures with different radii $(2.5, 5, 7.5, 10mm)$. 55

3.12 An example of gradient distribution calculated from one CT image. . . . 56

3.13 Illustration of the iterations of the FSP procedure with different settings of T_{stop} , while (a) T_{stop} = 0, (b) T_{stop} = 10, (c) T_{stop} = 100, (d) T_{stop} = 1500, (e) T_{stop}=15000, and (d) T_{stop}=20000. The regions of blood vessel are shown in red, and the candidates of SPNs are shown in green. With the growing of T_{stop}, the regions of the blood vessel are propagated and the FPs of SPNs are reduced. (e) shows the final segmentation result. . 58

3.14 Illustration of the change sensitivity of segmented pulmonary blood vessels with the different settings of T_{stop}. When setting the T_{stop} to 15,000, we obtained most sensible results. 59

3.15 FROC curve for nodule detection with parameter of ρ. 62

3.16 Examples of segmentation results of nodules connected to blood vessels. (a) shows original CT images, (b) shows true nodule regions painted in green. (c) shows segmentation results. Segmented nodules are shown in green; blood vessel regions are shown in red. 63

3.17 Comparison of BSE filter based on Gaussian kernel and surface fitting. (a) shows a chest CT slice with nodules painted in green. (b) shows the enhancement result of BSE filter based on surface fitting, and (c) shows the result of BSE filter based on a Gaussian kernel. Regions inside blue circles show incorrect enhancement at blood vessel regions 65

3.18 Illustration of blood vessel segmentation: (a) shows axial slice of input chest CT image, (b) shows the enhancement result of MS_LSE filter, (c) shows the segmentation result by region growing from initial blood vessels. Due to discontinuity, whole vessel tree cannot be segmented entirely (blue circles). Some nodules connected with vessels are incorrectly segmented (green circles). (d) shows the segmentation result of the proposed method. 66

3.19 Illustration of nodule segmentation: (a) shows axial slice of input chest CT image, (b) shows nodule candidates obtained by MS_LSE filter. The FP indicated by the arrow shows a regular sphere region. (c) shows a front surface terminating at the FP and indicates an irregular shape. . . . 68

3.20 Examples of FPs that occurred in the mediastinum region. The region marked by green shows two examples of the FPs. 69

4.1 The problems in the nodule matching and the solutions of the proposed method 72

4.2 Flowchart of the proposed methods. 74

4.3 Landmark segmentation. (a) Carina point, and (b) Rib bones (marking in green) 75

4.4 Examples of two CT images for nodule matching. The nodule "1" in I_a should match to the nodule "A" in I_b. The nodules "3" and "4" in I_a should integrate and match to the nodule "C" in I_b. 77

4.5 Illustration of matching pattern 1. Nodule "1" in image I_a matches nodule "A" in image I_b. However, although nodule "2" and nodule "B" exist nearly, they will not be considered as corresponding nodules, since their shapes are differ completely. 79

4.6 Illustration of matching $Pattern\ 2$. The nodule "3" and "4" in image I_a merge together and match to the nodule "B" in image I_b. 80

4.7 Illustration of matching $Pattern\ 3$. The nodule "5"in image I_a has no corresponding nodule in I_b, which is considered as non-corresponding nodule. 81

4.8 Illustration of $Constraint\ 1$. The distance between centroids of nodule "1" in image I_a and nodule "A" in image I_b is larger than $15mm$. The similarity calculation of these two nodules is skipped. 82

4.9 Illustration of $Constraint\ 2$. The distance between centroids of nodules "3" and "4" in image I_a is apparently lager than the sum of their radius. These two nodules are not considered to merge together and match to the nodule "C" in another image. 83

4.10 Examples of matching combinations. Combination 3 (Fig. 4.10(c)) is considered as the matching results of I_a and I_b. 85

4.11 Change of the numbers of nodule in follow-up CT images of three patients. 87

4.12 Examples of matching results. (a) and (b) show the examples of two normal corresponding nodules that are matched by $Pattern\ 1$, and (c) shows an example of merged nodules that are matched by $Pattern\ 2$. The nodules in the left image are combined and match to the nodule in the right image. 89
4.13 The examples of correctly matched nodules shown by volume rendering on follow-up CT images. 90
4.14 The false merged nodule. In the right image, a nodule was incorrectly merged with a FP. The merged nodule was considered to correspond to the nodule in the left image. 93
4.15 The change of matching rate with different settings of β. The best result was obtained when setting β to 0.2. 94

List of Tables

3.1 Acquisition Parameters of chest CT images 52
3.2 Pulmonary blood vessel segmentation results of 10 CT images using proposed method 57
3.3 TP rate and number of FPs on 20 standard-dose CT images using our proposed nodule detection method 60
3.4 TP rate and number of FPs on 20 low-dose CT images using proposed nodule detection method 61
3.5 Comparison of proposed method to conventional methods 62

4.1 Acquisition parameters of chest CT images 87
4.2 The nodule matching results of the proposed method 88
4.3 Comparison of the proposed nodule matching method to the previous method 90
4.4 Comparison of the proposed nodule matching methods to the method without the consideration of $Pattern\ 3$ 92
4.5 Comparison of the proposed nodule matching method to the method without consideration of $Constraint\ 3$ 94

Chapter 1

Introduction

In current medical diagnosis, treatment, and surgery, medical imaging plays one of the most important roles, since imaging devices such as Computed Tomography (CT), Magnetic Resonance Imaging (MRI), and ultrasound diagnostics yield a great deal of information about diseases and organs. However, radiologists have to analyze and evaluate a number of medical images comprehensively in a short time, which is a large burden. To lighten the burden, computer technology research has been used more often to analyze medical images in recent years. This field of research is called computer-aided detection/diagnosis (CAD) [1]. CAD is used to provide technical support to medical staff during diagnosis and treatment. In the absence of a doctor, CAD allows for the identification and possible emergency treatment of life-threatening symptoms. For instance, some hospitals use CAD to support preventive medical check-ups in mammography (diagnosis of breast cancer) [2], the detection of polyps in the colon [3], and lung cancer from CT images [4]. Our research aims to develop a chest CAD system using CT images. This dissertation introduces the approaches of automated segmentation of solitary pulmonary nodules (SPN), segmentation of pulmonary blood vessels and matching of segmented nodules.

This chapter introduces the main medical background of our research including lung anatomy (Section 1.1), lung cancer (Section 1.2), lung nodules (Section 1.3). Computer tomography (CT) is introduced in Section 1.4, including how lung tissue and diseases are observed on CT images, the role of CT in diagnosis and treatment of

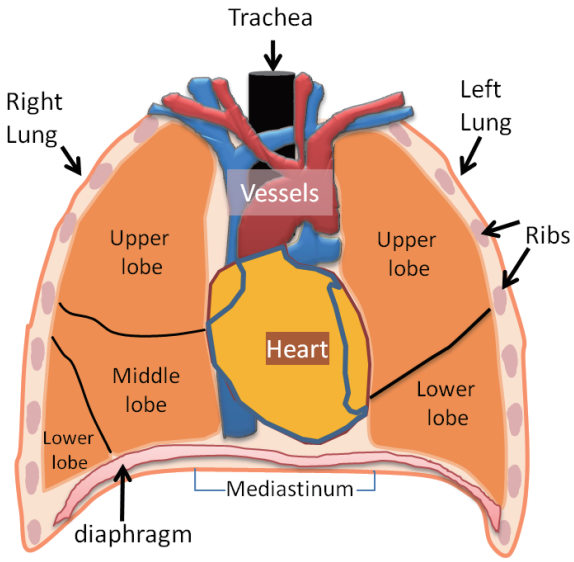

Figure 1.1: Illustration of lung anatomy in 2D.

lung diseases. Then, we introduce the benefits and problems of CT during diagnosis and treatment, which necessitate the development of a CAD system. The brief history and current status of CAD system are introduced in Section 1.5. Finally, the general structure of this dissertation is organized in Section 1.6.

1.1 Lung Anatomy

Figure 1.1 shows the illustration of lung anatomy in 2D. The lungs are a pair of large organs in chest, comprised of the right and left lungs. The two lungs are separated by a structure called the mediastinum (Fig. 1.1). The mediastinum contains the heart, the trachea, the esophagus, and blood vessels. Each lung is made up of sections called lobes; the right lung has three lobes, the left lung has two lobes and is smaller than right lung. Each lung has two layers of pleura covering the lungs and lining the inside of the chest. The lungs rest on the diaphragm: a wide, thin muscle that sits below the chest cavity and above abdomen, separating the two (Fig. 1.1). During a breathing cycle, the diaphragm contracts and relaxes, helping to fill and empty the lungs [5].

1.2 Lung cancer

1.2.1 Overview

Cancer (malignant tumors) is a generic term for a large group of diseases that can affect any part of the body [8]. One defining feature of cancer is the rapid creation of abnormal cells that grow beyond their usual boundaries, and can spread to other tissues or organs. The spreading process is called metastasis, and when a cancer has reached an advanced stage in which the malignant cells are attacking other organs, it is said that the cancer tumors have metastasized. The tumor in new organ is called metastases or metastasis cancer. The metastasis cancer always made up of cells similar to those of the original tumor (primary cancer) [6].

Lung cancer is a cancer that forms in lung tissue [7]. Since lung cancer tends to spread or metastasize very early in its course, it is a very life-threatening cancer and one of the most difficult cancers to treat [9]. According to World Health Organization (WHO) [8], lung cancer has been the most common cancer in the world for several decades. By 2008, there were approximately 1.61 million new cases, representing 12.7% of all new cancer cases. Lung cancer was also the most common cause of death from cancer, with 1.38 million deaths (18.2% of the total). Furthermore, Lung cancer remains a disease with a dismal prognosis. Although one-year all-stage survival is reported to have increased from 32% in 1973 to 41% in 1994, the five-year survival rate has remained unchanged at 14% [11, 15]. To find and treat lung cancer at an early stage is very important. This can lead to more treatment options, less invasive surgery, and a higher survival rate.

Cigarette smoking is the main cause of lung cancer [17]. Other causes for lung cancer may include genetic and environmental factors, such as passive smoking [18, 19], asbestos fibers [20, 21], radon gas [22, 23], familial predisposition. However, many lung cancer cases are not limited to a single cause, but a combination of factors.

1.2.2 Types of lung cancer

Cancer usually develops in the lungs in one of two ways: either by developing in the lungs or by spreading to the lungs. Cases that start in the lungs are categorized as primary lung cancer, and case that spread to the lungs from another part of the body are categorized as secondary lung cancer (the metastasis of cancer to the lungs). Primary lung cancer can spread to any organ in body. The liver, adrenal glands, brain, and bones are the most common sites for lung-cancer metastasis [9]. The lungs are also a very common site for metastasis from tumors in other parts of the body, such as the liver, kidneys and breast. In general, lung cancer mainly refers to primary lung cancer. Primary lung cancer is divided into two main types: (1) non-small cell lung cancer (NSCLC), and (2) small cell lung cancer (SCLC) [9].

1.2.3 Diagnosis of lung cancer

The majority lung cancer cases are diagnosed after a doctor requests testing for cancer based on a patient's medical history and the results of a physical examination. Lung cancer is usually first observed through chest radiography or chest CT images, as tumor nodules. To confirm the diagnosis, the tumor cells of nodules have to be examined under a microscope. The tumor cells are suctioned into the syringe by a biopsy, which is usually performed by bronchoscopy or CT-guided needle biopsy.

The details of diagnosis approaches of lung cancer are described as follows:

(1) Chest radiography [24]: Chest radiography is commonly called a chest X-ray. This technology employs ionizing radiation in the form of X-rays to generate a 2D image of the lungs. However, the sensitivity of standard chest radiography is too low to locate small tumors. Moreover, some studies have shown that the chest radiographys and sputum cytology do not effectively detect lung cancer in its early stages [25].

(2) Chest CT scanning [26]: CT scanning is usually performed as the second step to follow up an abnormal chest radiography to get more information about the extent

and/or location of tumors. CT scanning utilizes a series of x-rays to create a 3-dimensional view of the lungs. Since CT images are more sensitive than standard radiograph in the detection small tumors, it currently being researched for use as a screening tool for lung cancer.

(3) Bronchoscopy [27]: Bronchoscopy is a kind of endoscopic test, in which the lungs are viewed through a thin, flexible, illuminated tube with a tiny camera on the tip. When a tumor is discovered, the cell tissue can be obtained through the biopsy, which is located inside the tip of bronchoscope. Tumors located in the central areas of the lungs or in the larger airways are accessible via brochosopy.

(4) Needle biopsy[28]: If the tumors are located in the more peripheral of the lungs and are beyond the reach of a bronchoscope, a needle biopsy through the chest wall may be necessary. The biopsy is taken through a needle and inserted through the chest wall and into the tumor. Cells are suctioned into a syringe and are examined under a microscope.

1.2.4 Treatment of lung cancer

There are several different treatment options available for both primary and secondary types of lung cancer. The treatment choices for a given individual depend on the type of cancer (e.g., NSCLC, SCLC, metastasis), the location of the cancer, whether and where the cancer has spread, its stage (cancers are given a staging from 1 to 4 with stage 4 being the most aggressive) and the overall health status of the patient. Treatment for lung cancers can involve (1) surgical removal of the cancer, (2) chemotherapy, (3) radiation therapy or (4) combinations of these treatments [29].

1.3 Lung nodule

1.3.1 What is lung nodule?

A lung nodule, also referred to as a pulmonary nodule, is a mass of tissue located in the lungs. In 1996, the Fleischner Society published a glossary of terms specifically for chest CT [32] in which a lung nodule is defined as a "round opacity, at least moderately well marginated and no greater than 3 cm in maximum diameter." Lung nodules usually need to be at least 1 cm in size before they can be seen on a chest radiograph. A lesion should be considered as "nodule" if it satisfies the definition of nodule, which mainly considers the "nodular" morphology.

1.3.2 Relation between lung nodule and lung cancer

Lung nodules are very common and can be found at a rate of 1 in 500 in chest radiographs and 1 in 100 in CT scans of the chest [14]. Lung nodules can be either benign or malignant. The benign nodules include granulomas (clumps of inflamed tissue) and hamartomas (benign lung tumors). The most common causes of malignant lung nodules include lung cancer and metastatic cancer to the lungs (secondary lung cancer). However, lung nodules are less than a 40% [7] indicator for lung cancer and the majority of patients who have lung nodules do not show any symptoms.

Although the majority (at least 60%) of lung nodules are benign (not cancerous), early diagnosis of the cause of lung nodules is very important. This is because if lung cancer is caught early and is still small, there is a greater chance that it can be cured. The risk of a lung nodule being cancerous varies considerably depending on several factors. For example, in people less than 35 years of age, there is a less than 1% chance that a lung nodule will be cancerous, whereas it increases to more than 50% in people over age 50. Other factors that raise or lower the risk that a lung nodule indicates cancer include growth, size and shape of the nodule and the occupation and smoking history of the patient.

1.3.3 Types and shapes of lung nodules

In order to classify lung nodules depending on their locations, nodules are usually categorized into three kinds of nodules: (1) Isolated Nodules (nodules that are located inside the lungs, without any attachment), (2) Juxta-Pleural (nodules attached to the chest wall), and (3) Juxta-Vascular (nodules that are attached to the vessels that are inside the lung area). However, depending on the texture, lung nodules can be classified to four types: (1) Solitary Nodules (nodules that completely surrounded by the lung parenchyma and without associated pneumonia, atelectasis (lung collapse) or lymphadenopathies [12]), (2) Subsolid Nodules (semi solid nodules that have solid component within them that obscure the lung parenchyma), (3) Ground Glass Opacity (GGO, hazy opacity within the lungs that is not associated with obscured underlying bronchial structures or pulmonary vessels [13]), and (4) Cavitary nodule (nodule that contains an air-filled necrotic region is termed cavitary).

The most nodules have diameters between 3-30mm. The nodules vary in shape depending on type. Isolated nodules are usually spherical in shape (when viewed in 3D), and they are seen as circular objects in 2D cross sections. Attached nodules are usually semi-spherical.

1.4 Computer Tomography (CT)

1.4.1 History of CT

CT scans are a noninvasive, painless medical procedure. An overview of CT technology and its applications are presented in [30]. The first commercial CT scanner was invented by Sir Godfrey Newbold Hounsfield in 1971. Within several decades, CT has seen tremendous improvements [30, 31]. Current CT scanners consist of a radiation source and a set of detectors. The radiation source circles around the patient's body and the detectors measure the attenuation of the radiation of body at different angles. Then, computers are utilized to reconstruct slice images of the sections of the patient's

body from these measurements to provide a 3D view of body. These measurements also determine the CT values of the tissues in a CT image called Hounsfield unit (H.U.).

The images generated by CT scans are commonly composed of a matrix of 512×512 pixels in each direction with an image resolution as high as 0.3 mm per pixel. Doctors can obtain much more detailed information about tumors and organs from CT images than from traditional radiography imaging, which can only show 3D body structures as 2D images. Hence, CT images are being investigated as a screening tool for lung cancer to instead radiograph in recent years.

1.4.2 Lungs on CT

Generally, doctors use three kinds of cross sections to observe human body from one CT scan: axial , sagittal and coronal sections. We show examples of these three cross sections from a 3D CT volume of the lung in Fig. 1.2. Figure 1.2(a) shows one axial slice of a lung volume. From this slice we can observe the following components:

(1) Left and right lungs: Have large dark areas inside (air region).

(2) Trachea: A large spherical air region that located in the middle area of image. Trachea vary in size along the CT slices of the thorax, and diminishes completely when the trachea branches to the two bronchi.

(3) Rib bones: Elliipsodal regions with high intensity (CT value).

(4) Sternum: Similar to rib bone, only present in the top CT slices of the thorax.

(5) Mediastinum: The part in the thorax that contains the heart and is bound by the sternum from the front and spinal cord from the back.

(6) A cross section of a vertebra.

(7) Fat and muscle.

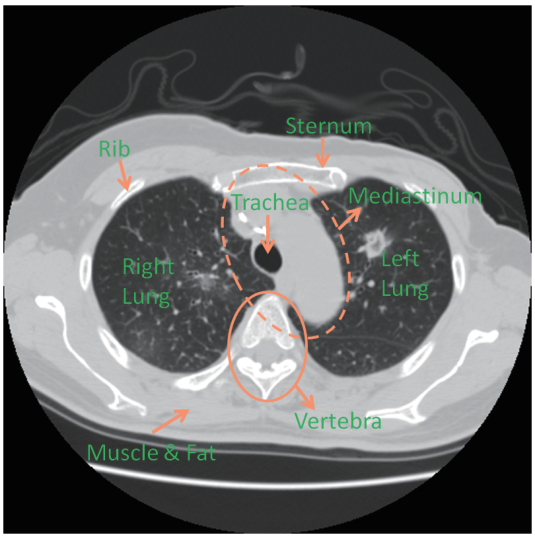

(a) Axial section

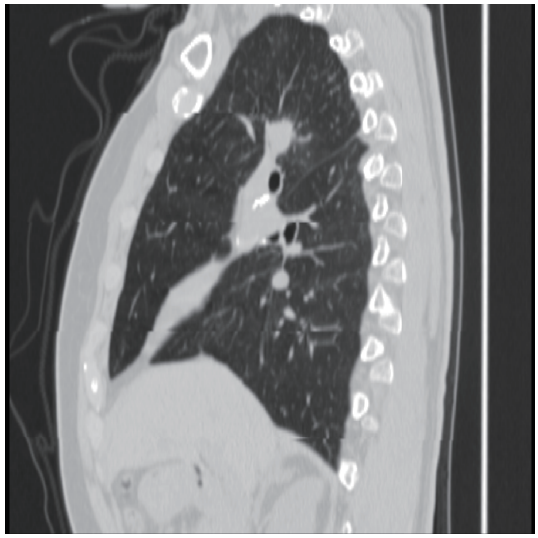

(b) Sagittal section

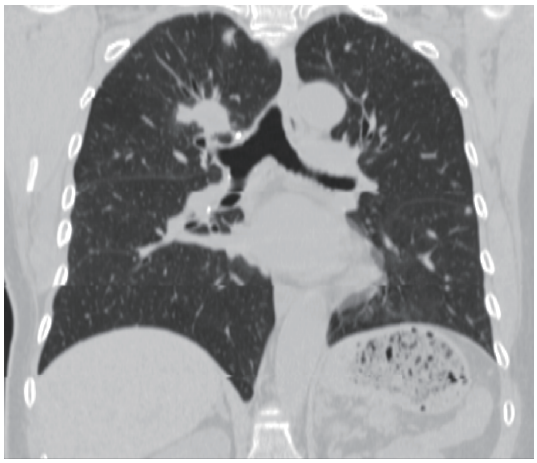

(c) Coronal section

Figure 1.2: Three separated axial sections of a 3D CT volume. (a) shows an example of an axial section, (b) shows an example of a sagittal section, and (3) shows an example of a coronal section of one CT volume.

1.4.3 Lung nodules on CT

The appearance of lung nodules in CT images can be described as compact lesions with relatively high contrast, circular shape and uniform density distribution. Compact nodules were found to have a Gaussian gray level distribution [33]. The gray level values of nodules in CT images are usually between -700 H.U. and 400 H.U., larger nodules often show larger CT values than smaller ones. Pulmonary blood vessels running perpendicular to the slices might appear to be circular in shape, and they usually have similar CT

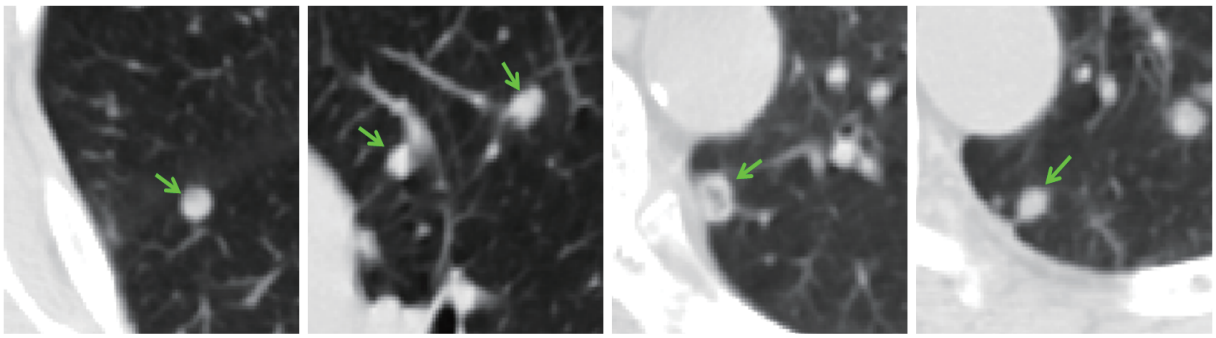

Figure 1.3: Illustrations of lung nodules on CT image. (a) shows a well-circumscribed nodule, (b) shows two vascularized nodules, (c) shows a pleural tail type, and (d) shows a juxtapleural nodule.

values to the nodules. Hence, in order to properly classify the nodules (especially the vessel-attached nodules) and blood vessels from CT images is an important and challenging work for radiologists. Lung nodules can be divided into four classes depending on their features in a CT as follows:

(1) Well-circumscribed: The nodule is located centrally in the lung, without significant connections to vasculature (Fig. 1.3(a)).

(2) Vascularized: The nodule is located centrally in the lung, but has significant vascularization (connect to neighboring vessels) (Fig. 1.3(b)).

(3) Pleural tail: The nodule is near the pleural surface, connected by a thin structure ("pleural tail") (Fig. 1.3(c)).

(4) Juxtapleural: A significant proportion of the nodule periphery is connected to the pleural surface (Fig. 1.3(d)).

1.4.4 Role of CT in the diagnosis and treatment of lung cancer (lung nodule)

Over the past several decades, CT scanning has become a key imaging modality for lung diseases. This is because CT images are more sensitive than standard radiograph in the

detection small tumors. At present, chest CT images are widely used to assist in both diagnosis and treatment of lung cancer (lung nodule).

(a) Diagnosis:

For the diagnosis of lung cancer, CT images have been used mainly in the early detection of lung nodules, the evaluation of lung nodules to determine whether it is solitary and whether mediastinal metastases are present, also to evaluate the mass by assessing its density [147]. Furthermore, the follow-up CT images are usually used to observe the growth of lung nodules or the metastatic situation. The navigation of lung nodules by using CT images is desirable for the further diagnosis of lung nodule such as bronchoscopy and needle biopsy.

(b) Treatment:

Chest CT images also can be utilized to assist the treatment of lung diseases. The information of lung cancer and the lung tissues around it that are observed in CT images is important for conducting the therapy plan. Furthermore, the follow-up CT images can be utilized to observe the the progress of chemotherapy and radiation in secondary lung cancer cases. To navigate the position of lung cancer by using CT images is also useful for several therapy approaches such as bronchoscopy and surgery.

1.4.5 Benefits and problems

(a) Benefits:

CT images can provide very detail information about organs and diseases though image slices in approximately 1mm of thickness. CT enables the radiologist to observe human's body through three different axial planes and a 3D view. Such benefits enable radiologists to detect lung nodules much earlier than conventional chest radiograph by using chest CT images.

(b) Problems:

The first problem of CT scan is the high risk due to radiation exposure. Secondly,

high resolution image cause an dramatic increase of the number of image slices, which rapidly increases the burden on radiologists, and causes high miss rates of radiologists in detecting lung nodules at a early stage. To lighten such burden, research in computer-aided detection/diagnosis (CAD) is predicted to develop rapidly. CAD systems are desirable as a "second opinion" to assist radiologists to improve the performance of detection and observation of diseases in screening [48]

1.5 CAD system

1.5.1 Overview

The CAD system includes the procedures of computer-aided detection (CADe) and computer-aided diagnosis (CADx). A CAD system is desired to detect conspicuous structures (CADe) and evaluate such structures (CADx) from medical images. Also, CAD systems are expected to assist doctors in analyzing the effectiveness of treatment and give opinions to the therapy planning.

CAD has been defined as diagnosis made by a physician who takes into account the computer output based on the quantitative analysis of medical images [48]. This concept is clearly distinct from automated computer diagnosis, which was firstly introduced in the 1960's [34, 35, 36], and developed in 1970's [37, 38]. Automated computer diagnosis was generally assumed to be a technology to replace radiologists in detecting abnormalities. However, because of the limitation of the power of computers and image processing techniques at the time, these early attempts were not successful. Then, in the 1980's, another definition which assumed that "the computer utilized by radiologists, but not replace them" was emerged. This is because the computer cannot and may not substitute the doctor, but rather plays a supporting role, doctors (generally radiologists) are always responsible for the final interpretation of a medical images. This concept is currently known as computer-aided detection/diagnosis (CAD). The basic concept of CAD is to provide a computer output as a "second opinion" to assist

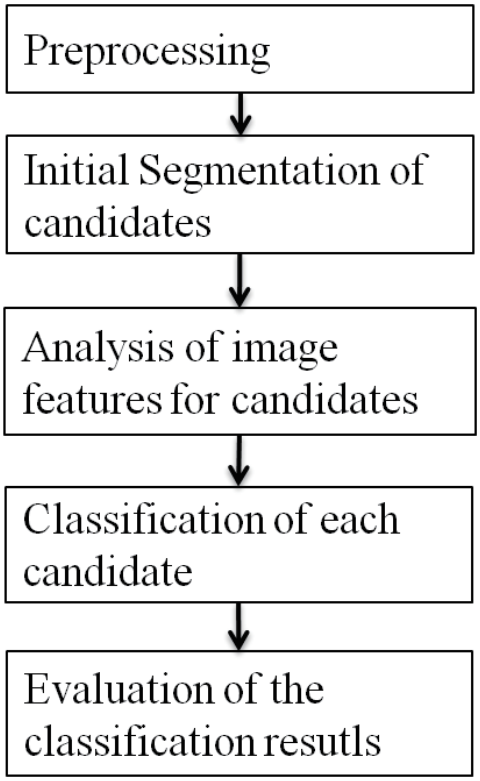

Figure 1.4: Illustration of the general framework of the CAD system.

radiologists in the interpretation of medical images by improving the accuracy and consistency of radiological diagnosis and also by reducing the image reading time [48]. Since then, CAD has been developing quickly and widely, and has been extended to various medical imaging modalities including mammograms, radiograph, CT and MR [39, 40, 41, 42]. Recently, this research field has become one of the major research topics in medical imaging and diagnostic radiology [43, 44, 45, 47].

1.5.2 General framework of CAD

Figure 1.4 illustrated the general framework of the CAD system. The basic technologies involved in the CAD system are:

(1) **Preprocessing :** The preprocessing usually performs the reduction of image noise or artifacts and the extraction of the regions of interest (ROIs).

(2) **Initial segmentation :** The initial segmentation performs a rough segmentation of the initial target regions (candidates) in the ROIs.

(3) **Analysis of image features for candidates :** The analysis of image features is implemented for each candidate after the initial segmentation. The features include compactness, size, location, average intensity (gray scale level value), and so on.

(4) **Classification of each candidate**: The classification of each candidate is applied after the feature analysis. The candidates are classified into true positives (TPs, the final target region) or false positives (FPs).

(5) **Evaluation**: The evaluation of classification results is implemented to observe the performance of the CAD system. The receiver operation characteristic (ROC) analysis is usually utilized to conduct the evaluation.

1.5.3 Current status of CAD

CAD technology can be applied to a wide range of modalities and used for all parts of the human body such as the skull, thorax, heart, abdomen and spine. However, the majority of CAD schemes that have been developed so far include breast CAD on mammograms, colon CAD on CT colonography (CTC), chest CAD on chest radiograph and CT image. The details of these three kinds of CAD are described as follows.

1.5.3.1 Breast CAD system on mammogram

The breast CAD systems on mammogram are developed to aid radiologists in detecting of mammory lesions that may indicate the presence of breast cancer. There are two types of breast CAD systems based on mammograms: one is based on conventional screen-film mammograms and another one is based on digital mammograms [2]. The first type requires the scanning and digitization of films. These are then saved to computer for further analysis. The second type uses full-field digital mammographic (FFDM) technology. Although the FFDM is recognized as being superior to the con-

ventional one, the results obtained in recent studies show that there is no difference in accuracy between FFDM and the conventional methods [49, 50].

The first commercial CAD system for mammography was developed by R2 Technology based on the technique from a research group at the University of Chicago (USA). A number of commercial breast CAD systems on mammograms are currently available for clinical use [51, 52]. Several researchers have reported that the accuracy of interpretation of screening mammograms with CAD systems is better than the accuracy without CAD [53, 54]. However, a few studies also show that the performance of current commercial breast CAD systems still need to be improved [55].

1.5.3.2 Colon CAD system on CTC

Colon CAD can be employed as a second reader to aid in detecting polyps and masses from CT colongraphy (CTC). CTC is a non-invasive screening technique with promising results for the detection of polyps and small tumors [56, 57]. However, three factors limit the widespread use of the technique, especially for screening purposes: (1) the need for colon cleansing, (2) the readers expertise required for interpreting examinations, (3) and the unknown diagnostic performance when applied in a mass screening program [60]. To deal with these drawbacks, Coin et al. reported their research on computerized radiology of colon CTs [58] in 1983. In 1994, Vining et al. introduced research on visual colonoscopy using CT images [59]. Since then, research on colon CAD for polyp detection has been developing quickly [3, 61, 62]. Presently, commercial colon CAD systems such as Ziosoft [63], GE [64], Siemens [65] are available for clinical applications.

A colon CAD scheme typically consists of the (1) segmentation of colonic walls, (2) the generation of intermediate polyp candidates, (3) the classification for the detection of final candidates, and (4) the presentation of the polyp candidates. The remaining tasks for the radiologist is the validation or rejection of the polyp candidates. Sosna et al. reported that the performance of colon CAD ,especially in terms of sensitivity, is comparable that of a human reader [68]. However, in order to confirm the performance

of current colon CAD systems, further examination by larger databases, evaluated retrospectively and prospectively is required.

1.5.3.3 Chest CAD system

The most important application of chest CAD systems is the ability to detect and characterize lung nodule. A number of researches have devoted time to the construction of CAD systems in the last two decades [69, 71, 72, 73, 75, 81, 114]. Since the chest radiography is the most common image examination approach for lung diseases, many chest CAD systems focused on detection of the lung nodules from chest radiograph [39, 72, 74, 75]. However, CT image provides much more information about diseases than conventional radiograph, and several researches show that CT image can detect four times the number of malignant lung nodules and six times the number of stage I malignant nodules than chest radiography [77, 78, 79], which strongly suggests the use of CT scan over chest radiography for lung cancer screening. Construction of chest CAD systems based on CT images has become the most popular topic in this field [85, 88, 90, 117, 120].

The previous chest CAD systems developed for CT images focused mainly on the automated detection of solitary pulmonary nodules (SPN). Recently, there has been more work on the classification of malignant and benign SPNs [92]. Since the progress of lung cancer is observed in relation to the change of shape and the number of pulmonary blood vessels, the segmentation of pulmonary blood vessels is also crucial for a chest CAD system. The doctors usually utilize the follow-up CT images of a patient to observe the growth or the effectiveness of treatment in nodules. However, patient position on the CT table as well as a patient's heartbeat can make follow-up CT images hard to read due to the deformations. This is particularly true in the case of secondary lung cancer where hundreds of SPNs may occur, since finding of the corresponding nodules from hundreds of SPNs on two follow-up CT images makes greatly burdens to physicians. Therefore, the automated nodule matching method is also desired in chest CAD systems.

1.6 Organization of this thesis

Our research aims to develop a novel chest CAD system. This dissertation introduces the two main focuses of our research: 1) Automated segmentation of lung nodules and blood vessels; 2) Automated matching of segmented lung nodules. In this dissertation, the proposed segmentation method aims to improve the performance of both lung nodule and blood vessel segmentation by incorporating these two segmentation procedures. The proposed nodule matching method aims to find all the corresponding nodules from follow-up CT images. This dissertation is comprised of five chapters.

Chapter 1 introduced the background of our research. The main medical background including the diagnosis and treatment of lung cancer, lung nodule, and CT were described. Then, we introduced the brief history, general framework and current status of CAD system.

Chapter 2 introduces the main approaches involved in a chest CAD system. Then, a related work review is described, which introduce the current segmentation methods of lung nodules and pulmonary blood vessels, matching methods of lung nodules. The purpose and basic idea of this dissertation will be presented following the discussion of the disadvantages of current approaches.

The following two chapters are the main body of this dissertation. Chapter 3 introduces an improved Hessian and level set-based methodology for segmentation of both lung nodules and vessels. The main goal of a nodule segmentation method is to provide a low number of FPs per case as well as high sensitivity. Since the FPs mainly occur in blood vessel regions in the initial nodule candidates detection processing. The key-point is how to discriminate between nodules and blood vessels. To solve this problem, the proposed method incorporates the initial vessel regions and nodule candidates into a fine segmentation procedure to obtain sufficient segmentation results. Chapter 4 introduces a novel methodology for the automated matching of segmented nodule from follow-up chest CT images. The proposed method can address the matching of temporally changed nodules, which is the challenging topic in this field.

In chapter 5, we conclude this thesis on the development of a chest CAD system. Several aspects and potential limitations of the proposed techniques are summarized. Furthermore, various future works and promising research directions are discussed for the further developments of chest CAD system.

Chapter 2

Technique and related work of chest CAD system

This chapter introduces the main techniques involved in development of a CAD system, including segmentation, classification, registration. Related work in terms of nodule segmentation, blood vessel segmentation, and nodule matching are also reviewed. The purpose and basic principals of this dissertation are presented following the discussion of the disadvantages of previous approaches.

2.1 General techniques

In this section, we introduce the general techniques of medical image analysis in the development of CAD systems. The key concepts are medical image segmentation, classification, and registration.

2.1.1 Medical image segmentation

Medical image segmentation refers to techniques to partition an image into regions and delineate the anatomical objects of interest in the image, discriminating each object from other objects and from its background. Several computer vision techniques have been applied to a range of medical imaging modalities to execute the segmentation. The common approaches to medical image segmentation include but are not limited

to classical image analysis techniques, deformable model fitting techniques, atlas-based segmentation.

(1) **Classical image analysis techniques:** Standard image processing algorithms such as thresholding, region growing, edge detection, morphological operators and filters are the fundamental approaches to segment an image into several separate regions. Rogowska et al. provided a introduction of several medical image segmentation methods using such standard imaging techniques [93]. Since such fundamental image segmentation methods are sensitive to noise and are usually insufficient for performing fine segmentation, these image analysis techniques are commonly used in the preprocessing or initial segmentation.

(2) **Deformable model fitting technique:** Deformable model fitting is defined as the problem of finding the optimal configuration of a parameterized shape model that best describes the object of interest in an image. In contrast with rigid patterns or template matching methods, deformable models allow the model to be deformed to fit the evidence within the image, albeit within certain limits [94]. The deformable models such as active contours [95], active shape models [96], active appearance models [97], and level sets [98] have been utilized to many medical image segmentation. These techniques fit the model to the image data via optimization methods using energy or cost functions that evaluate the quality fit. Since the deformable model fitting techniques attempt to find boundaries of regions, such techniques are often employed to execute the fine segmentation.

(3) **Atlas-based segmentation:** The atlas-based segmentation techniques attempt to segment objective structure in a new image by drawing a correspondence between this new image and a previously constructed atlas. The atlas is often the representative or average of the variations in the anatomy [94]. A matching process is performed to find the correspondence by similarity calculation. Various atlas-based segmentation methods have been reported to segment organs from brain MR images, chest and abdomen CT images, and so on. Such techniques have the

advantage of being robust in the presence of disease [100].

2.1.2 Classification

The classification techniques are widely used in medical image analysis for classifying foreground (regions of interest, e.g., lung nodules, colon polyps) and background regions on medical imaging modalities. Classification-based techniques attempt to label individual pixels or regions with labels for the anatomical structure of interest [94]. These techniques usually use a classifier to predict the membership of specific classes by analyzing features of pixels, regions, or an entire image. The classifier was developed using pattern recognition and machine learning techniques [101, 102]. However, such technique requires experts to devise useful features and gather a sufficient amount of data for training the classifier.

Another classification technique in terms of the graph cats-based segmentation [99]. The graph cuts classify each pixel within the image as either belonging to the foreground representing the desired object or the background. This technique has good performance on segmentation without requiring large amounts of labeled data to induce the classifier. However, the graph cuts based method requires to define complex cost functions, similar to the model-fitting techniques.

2.1.3 Registration

Image registration is a fundamental task in medical image processing used to match multiple images taken, for example, at different times, with different sensors, or from different subjects. Basically, image registration transforms different data sets into one coordinate system, and provides basis for image comparison and information integration in many clinical applications. One of the images is referred to as the reference image and the second image is referred to as the target. Image registration involves spatially transforming the target image to align with the reference image.

Image registration algorithms can be classified into intensity-based and feature-based [103]. Intensity-based methods compare intensity patterns in images via cor-

relation metrics, while feature-based methods find correspondence between image features such as points, lines, and contours. According to the transformation models for transforming the target image space to the reference image space, image registration algorithms can be classified into rigid (or linear) and non-rigid registrations. The rigid registration model includes translation, rotation, scaling, and other affine transforms. Rigid registration is global in nature and only can be used to compensate the inelastic deformations. Non-rigid registration is capable of locally warping the target image to align with the reference image, thus, can be used to compensate the elastic deformations.

Medical image registration is one of the most active research areas in medical image analysis [104, 105, 106], which often involves non-rigid registration to deal with elastic deformations. Rueckert et al. introduced a non-rigid deformation using cubic B-splines-based free form deformation [107]. Mutual information was applied as a similarity criterion in a hierarchical multi-resolution framework. Mattes et al. [108] utilized a similar technique to perform the inter-modality registration. PET and CT chest scans were registered in their report.

2.2 Purpose of our research

We aim to develop a chest CAD system for lung nodules, which includes the functions such as automated lung nodule segmentation, pulmonary organs (e.g., blood vessel) segmentation, automated lung nodule matching, and can analysis the malignancy, nodule metastatic situation or therapy effect from the segmentation and matching results. Figure 2.1 shows the illustration of the CAD system.

The works introduced in this dissertation focus on lung nodule segmentation, pulmonary blood vessel segmentation and nodule matching.

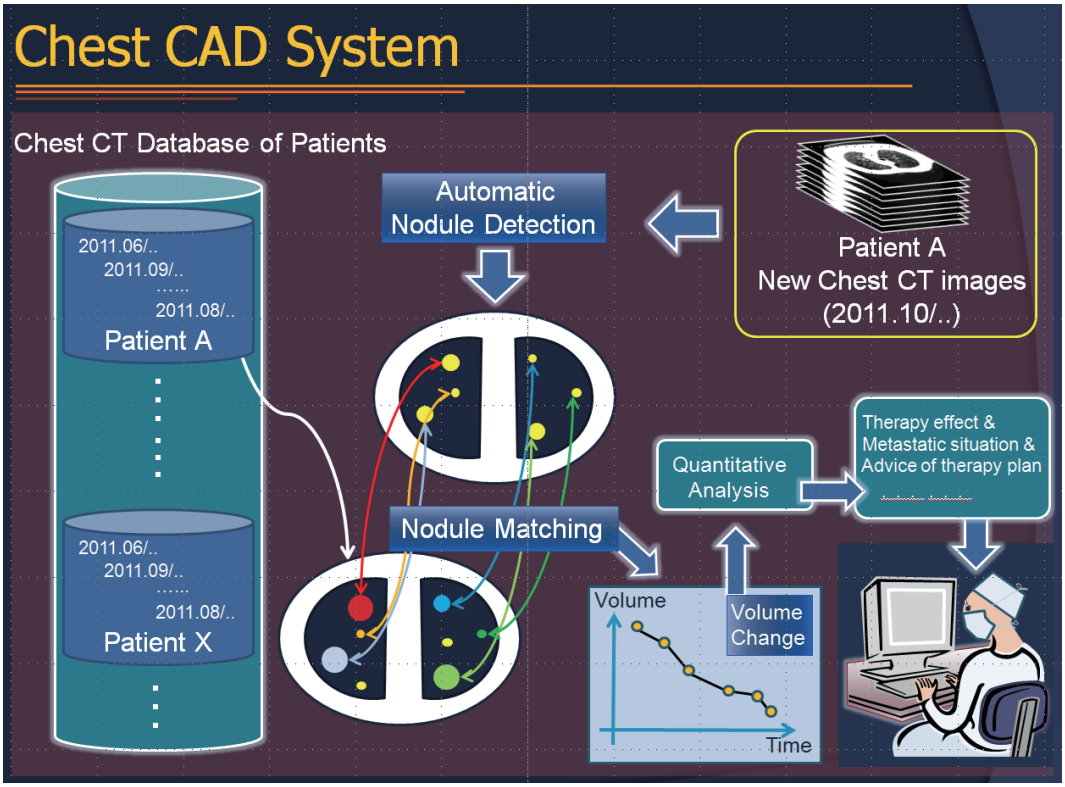

Figure 2.1: The illustration of the developing chest CAD system. A chest CT database is constructed to storage the follow-up CT images of all the patients. All of the CT images in the database are processed by the segmentation of nodules and organs, and the automated matching of segmented nodules. When a new CT image of one patient is generated, the automated segmentation of nodules and organs will be executed on it. Then, automated nodule matching between the current CT image and the last CT image in the database is performed, and the report of nodule growth can be obtained from the matching results. By analyzing the nodule growth and other information recorded in the database, the system can give several suggestions for the treatment, metastatic situation and therapy planning.

2.3 Related work

This section reviews related works on lung nodule segmentation, pulmonary blood vessel segmentation and nodule matching.

2.3.1 Lung nodule segmentation

Due to clinical importance, the automatic detection of SPNs in chest CT images has become a common research topic, the number of such articles has roughly doubled each year in recent years. Lung nodule detection systems generally consist of some common steps: (a) image preprocessing; (b) nodule candidate detection; (c) false positive reduction; (d) nodule characterization. The image preprocessing step usually performs a lung area extraction scheme to restrict the processing area of nodule detection and performs a smoothing procedure to reduce noise and image artifacts. So far, many methods have been developed to generate nodule candidates, but there are always many false positives among these candidates. Thus, the second step focuses on the FP reduction. The nodule characterization step mainly shows the likelihood of malignancy of a nodule. Steps (b) and (c) of nodule detection systems will be covered below.

2.3.1.1 Nodule candidate detection method

Thresholding is the most common technique for initial nodule detection. Many methods reported attempt to identify initial nodule candidates directly from the input CT images by use of a single thresholding process [82, 83, 84]. Armato et al. introduced a multiple thresholding method to detect initial nodule candidates [85, 86]. Zhao et al. also introduced a method that employs thresholding to indentify the initial nodule candidates, and reported a sensitivity of 94.4% with 906 false positives per CT image [87]. However, such thresholding techniques often cause a large numbers of FPs and may miss low-contrast nodules.

Model-based methods are also reported for initial nodule candidate detection. Takizawa et al. [91] utilized 3D geometrical models to identify nodules and other structures in lungs such as blood vessels and lung parenchyma. A template matching method [81] using a nodular model based on intensity distribution is reported, which is feasible for nodule detection. McCulloch et al. [89] developed a CAD system that consisted of two subsystems. The first sub-system further consisted of a multi-stage modeling architecture for the identification and classification of different regions, including nod-

ules, blood vessels, lung parenchyma, and scars, The second sub-system was a Bayesian model selection architecture in which the alternative representations of the regions inside the lungs to determine the most probable model of the underlying data. Regions for which the nodule model provided the highest probability among all models were considered to be suspicious nodule candidates, and others were considered to be non-nodule candidates.

The blob structure enhancement (BSE) filter are confirmed have good performance for the initial nodule detection [47, 80, 111, 112, 113, 144], since the nodules often show blob-like shapes. The application of a BSE filter as a preprocessing step would be advantageous for the initial detection of nodules, since such filters are also sensitive to the low-contrast nodules or those connected to blood vessels or airway walls. Most of such enhancement filters are Hessian-based, and were firstly introduced by Lorenz et al.[109] and Sato et al. [110]. Li et al. [80] developed a selective enhancement filter for simultaneous enhancement of nodules and suppression of other normal anatomic structures such as blood vessels and airway walls, which were the main sources of false positives for nodule detection in CT. They reported a sensitivity of 93.4% (71/76) and a false-positive rate of 4.2 per section. Paik et al. [113] also employed a BSE filter for initial nodule detection based on the surface normal overlap. Their filter outputs a score for each voxel that is proportional to the number of surface normals that pass through the neighborhood of the voxel, and the score for blood vessels is generally lower than that for nodules.

Other CAD schemes for detection of initial nodules includes shape index and curvedness-based [114], weighted k-means clustering-based[88] and so on. Bae et al. [115] developed a CAD scheme for detection of nodules in three categories: isolated, juxtapleural, and juxtavascular nodules.

For initial nodule identification, the definition of a criterion for determining whether a true nodule is correctly identified and the performance level for initial nodule identification because it is an important step of the entire CAD system [4]. The above described methods may have good performance level for detecting SPNs in input CT images, but

they often cause many FPs at normal pulmonary structures, such as the bifurcation parts of blood vessels. Hence, FP reduction is required.

2.3.1.2 False positive (FP) reduction

Pattern recognition approaches that include feature analysis and classification are the most common approaches for FP reduction [74, 86, 88, 90, 113, 114, 115, 120]. Features as compactness, sphericity, average intensity value, 3D curvature, and texture are often utilized to distinguish nodules from FPs, while rule-based classifiers, fuzzy classifiers, neural networks, k-nearest-neighbour (kNN), support vector machine (SVM) and Bayes classifiers are usually utilized to execute the classification.

Many research groups reported the utilization of rule-based classifier, which is simplest to distinguish the actual nodules from FPs [113, 115]. However, the rules were generally determined manually and empirically in existing CAD schemes, which leads to tediousness, long design time and over-training. Li et al. [116] devised an automated method based on the rule-based classifier, which can minimize the over-training .

Researches that perform FP reduction by artificial neural network (ANN) [117, 118] or improved ANN based method [119] have been reported. These methods showed better performance than the rule-based classifiers. Murphy et al, [114] proposed a kNN-based method and detected 80% of annotated nodules at an average of 4.2 false positive detections per scan when tested on 810 CT images. Hardie et al., [121] compared a Gaussian Bayes linear classifier, a Fisher linear discriminant (FLD) classifier and a quadratic classifier.

Besides, since many FPs in nodule detection are produced in the blood vessel regions, some research has focused on FP reduction by removing the overlap between blood vessel regions and nodule candidates [122, 123].

A study called "Automatic Nodule Detection 2009 "(ANODE09) (van Ginneken et al.[124]), which compared the performance of the several proposed CAD systems using a common database and common evaluation protocol. The methods [90, 114, 117, 118] were introduced in ANODE09 online CAD challenges for the detection of pulmonary

nodules.

2.3.2 Pulmonary vessel segmentation

Segmentation of pulmonary blood vessels from chest CT image is required because of its importance for clinical tasks such as the diagnosis of vascular diseases or the tumors that are connected with blood vessels. The relation between the nodules and blood vessels also provides very useful information for the diagnosis and treatment of lung cancer. The segmentation and characterization of blood vessels is often a prerequisite for diagnosis, treatment planning, and follow-up studies in clinical applications.

Region growing-based methods [125, 126] are conventional approaches of blood vessel segmentation. Some blood vessel centerline segmentation methods were proposed by using skeletonization techniques [127] or ridge extraction techniques [128]. Centerline extraction results can be used to reconstruct vessel trees. Mathematical morphology scheme-based blood vessel extraction approaches have also been proposed [129, 130]. They utilize the morphological operators that can keep the blood vessel regions and eliminate unwanted regions. Some parametric deformable models such as active contours (Snakes) [131, 132] and geometric deformable models (level-sets) [133, 134] can also be used to extract blood vessels by following some shape features or the intensity distribution of vessels. In recent years, Hessian-based LSE filters are being widely utilized for the segmentation of blood vessels. Poli et al. introduced an algorithm based on multiple oriented linear filters that is sensitive for the segmentation of blood vessels with different orientations and thicknesss [135]. Sato et al [110] proposed a multiple scales LSE filter that is based on the eigenvalues of the Hessian matrix, and some similar research was introduced [136, 139].

2.3.3 Lung nodule matching

By utilizing of the sequential follow-up CT images, early changes in nodule size and numbers can be assessed [146]. Hence, follow-up chest CT images are a well-established means of evaluating lung disease progression or effectivity analysis of the treatment of

metastatic lung cancer [147]. However, to identify subtle changes of lesions from two different CT images is very difficult for radiologists. This is because thin-sectioned CT images often generate a large number (typically 300-500) images of 1 mm sections, and the lesion usually involve overlap with anatomic structures such as vessels, the heart and the diaphragm. Especially, in the case of metastatic lung cancer, hundreds of SPNs may occur. Furthermore, the different poses of a patient on the CT table as well as the effects of heartbeats and respiratory motion usually causes the deformations on follow-up CT images. Thus, the automatic matching of lung nodules from follow-up CT images is required for a CAD system and also is useful for radiologists performing follow-up screening.

The methods of nodule matching can be generally classified into two categories: (a) Category 1: To find the matching nodule in current (past) scan of a mouse click-specified nodule in past (current) scan [148, 150, 151], and (b) Category 2: To find all the matching nodules specified by automatic segmentation in two scans [154, 155, 157, 159].

(a) Category 1:

The methods belong to Category 1 only focus on finding the matching nodule of one specified nodule.

Sun et al. proposed a semi-rigid model for the registration of lung nodules [148]. Their method considers principal structures surrounding the nodule and allows relative movements among the structures. A similarity metric, which evaluates both the image correlation and the degree of elastic deformation amongst the structures, is maximized by a two-layered optimization method, employing a simulated annealing framework.

Cheng et al. tested a matching program that is included in a commercial CAD system (LungCARE VE31E, Siemens Medical Solutions [149]) to perform the nodule matching [150]. The nodule matching operation begins with the computation of approximate longitudinal (e.g., z-axis) global alignment between two serial

sets of CT images. Refined alignment parameters are then calculated on the basis of the cross-sectional area of the lungs and the position of the trachea. Surface points of all surrounding objects are extracted and used to create a distance map. Points in the follow-up set of CT images are superimposed onto the distance map for the baseline set and then shifted in three directions to search for the optimal correlation between the two sets.

Blaffert et al. compared several registration techniques for nodule matching [151].

(b) Category 2:

The methods belonging to Category 2 focus on the automatic matching of all the nodules in two follow-up CT images. Kusanagi et al., proposed a method to find pairs of corresponding nodules by representing nodule position as a relative coordinate in the lung region [152]. Kubo et al. proposed a method to find corresponding slice positions from two CT images for comparative readings of CT images taken for mass screening [153]. They employed a template matching process for matching the lungs, heart, aorta and blood vessels and find nodule pairs in accordance with the relative position of each nodule in the lung region and their distance.

Betke et al. used the rigid affine registration and the iterative closest-point (ICP) algorithm to develop a global nodule registration system [154]. They utilized anatomical landmarks such as the sternum, vertebrae and tracheal centroids for initial global registration. Such initial alignment is then refined by an iterative closest point (ICP) process. Hong et al. introduced a multi-step nodule registration method by iterative surface registration and smallest euclidean distances [155]. Reeves et al. used a 3D rigid affine transformation for the registration of small volumes of interest containing nodules whose localization and size were predetermined using a 3D template matching method [156]. Since their emphasis was nodule growth rather than registration, quantitative results on registration accuracy were not described. Some non-rigid registration-based methods are also

introduced [157, 158]. The non-rigid registration has better performance than rigid and semi-rigid registration for registration of lungs since they can address the compensation of elastic deformation.

2.4 Disadvantages of previous methods

This section summarizes the main problems of current chest CAD systems. Particularly, we will focus on the limitations of methods for lung structure segmentation and lung nodule matching. The main limitations are discussed in the following paragraphs.

(a) Lung nodule segmentation:

The current available nodule segmentation methods suffer from the following problems:

(1) Classification of nodules and blood vessels: This problem remains challenging. Due to the low contrast of the intensity between nodules and blood vessels in CT images, detection of the nodules that connect with blood vessels and the reduction of FPs around blood vessel bifurcations remain a main problem in nodule detection methods.

(2) Selection of effective feature: The current learning-based FP reduction methods usually have good performance for reducing FPs. However, too many different features were introduced for the learning phase. Finding reliable features is still difficult. Usually, the incorrect reduction of actual nodules (both attached and isolated types) is unavoidable due to unreliable feature selection.

(b) Segmentation of pulmonary blood vessel:

The problems of current available pulmonary blood vessel segmentation methods are shown following:

(1) Avoidance of disconnected segmentation on the small bifurcation point: The pulmonary blood vessels show a complex tree structure that branches and be-

comes smaller from the lung hilar toward the periphery of the lung. Disconnection point of the pulmonary vessels may occur in the CT data, particularly on small bifurcation points. Hence, segmentation of the whole pulmonary blood vessels trees is still challenging.

(2) Classification of the vessels and other structures: To avoid incorrect segmentation of non-vessel structures such as the chest-wall, heart and nodules that connect with blood vessels is still difficult.

(c) Nodule matching:

The methods belonging to Category 1: Usually run fast but difficult to handle the elastic deformation due to breath or heartbeat. Also, if there are many SPNs in a patient, matching them by the methods in Category 1 is time-consuming.

The methods belonging to Category 2: Matching accuracy depends on nodule detection. If there are too many FPs detected, the actual SPNs in one CT image may be incorrectly matched to the FPs in the second scan. Furthermore, due to the growth of nodules and the effect of chemotherapy, merged/separated or appeared/disappeared nodules may occur. To match such nodules remains challenging using previous methods.

2.5 Basic ideas in this dissertation

Figure 2.2 shows the illustration of the basic ideas and the disadvantages of previous methods to be solved in this dissertation. We aim to improve the segmentation accuracy of both of SPNs and pulmonary blood vessels by segmenting them separately and simultaneously. Also, segmentation of finely connected pulmonary vessel trees is important. For the nodule matching, we propose a method that can automatically find all the matching nodules from nodule segmentation results (belonging to Category 2). We aim to deal with the two main limitations of the previous matching methods: 1) avoidance of false matching, which might incorrectly match an actual nodule to a FP from two

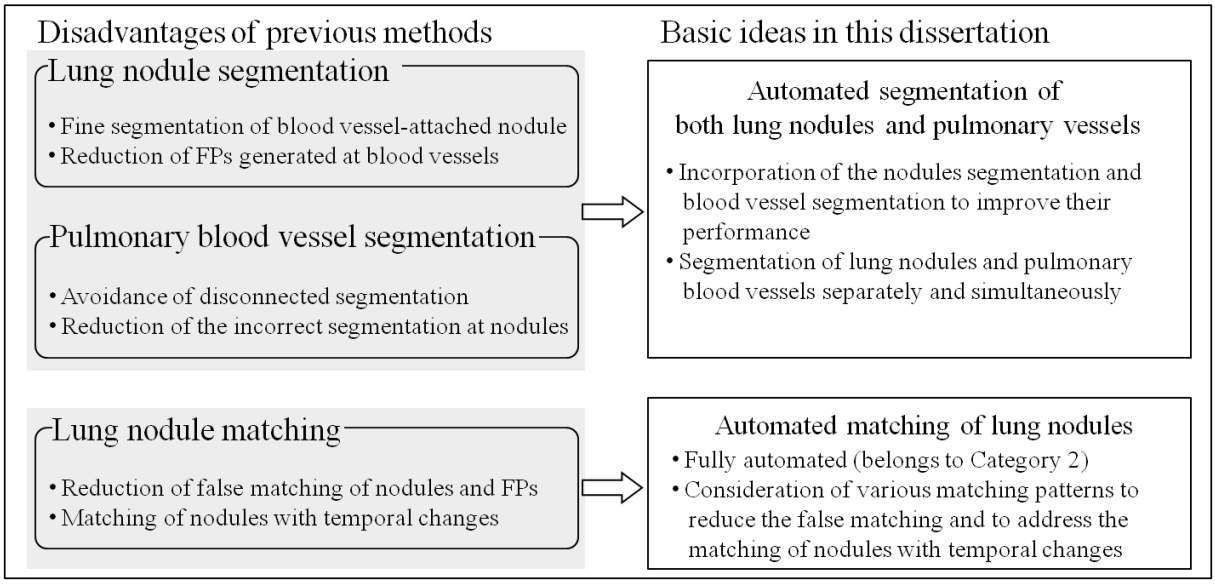

Figure 2.2: Illustration of the basic ideas and the disadvantages of previous methods to be solved in this dissertation.

follow-up CT images, and 2) matching of the nodules with temporal changes.

The basic approaches and ideas in this dissertation focus on:

(1) Fine segmentation of both SPNs and pulmonary blood vessels:

We utilize Hessian matrix-based LSE and BSE filters across multiple scales to enhance the line-like and blob-like structures as the initial blood vessel regions and nodule candidates, respectively. The conventional methods focus on employing only BSE or LSE filters to execute the initial segmentation of nodules or blood vessels. However, due to similar intensity, incorrect discriminations between nodules and blood vessels may occur in the enhancement results. To obtain sufficient segmentation results of both the blood vessels and the nodules, we will utilize both BSE and LSE filters, and incorporate their enhancement results into a fine segmentation process of both pulmonary nodules and blood vessels. Fine segmentation is performed by a front surface propagation (FSP) procedure that is based on the fast marching method (FMM) (extended from the level set method [98]). The initial vessel regions and nodule candidates are incorporated into the FSP procedure to make the front surface cover the blood vessels with suppressed

nodules. Consequently, the regions covered by the front surface are considered extracted pulmonary blood vessels, whereas the nodule detection result is obtained by removing the nodule candidates covered by the front surface.

(2) Automated matching of segmented nodules:
The rigid and non-rigid registrations can be utilized to compensate for the inelastic and elastic deformations respectively of follow-up CT images. The corresponding nodules are found based on similarity calculations between the nodules of two different CT images. In order to reduce the false matching between actual nodules and FPs, we will utilize the features including position, average intensity, and diameter of nodule for the similarity calculation. This potentially has better performance than the previous work [158], which only used the position of nodule. Furthermore, by considering the temporal changes of nodules, such as merger/separation and appearance/disappearance, we introduce three different patterns of similarity calculation to compensate such temporal changes.

2.6 Main contributions

2.6.1 New approaches

This dissertation introduces a new approachfor the automatic segmentation of SPN and pulmonary blood vessels, which can segment them finely and separately. Also, a new approach for nodule matching is introduced. The new approach for nodule and vessel segmentation that employs the Hessian-based enhancement filter and level set-based front surface propagation is described in Chapter 3. Then, a nodule matching method based on rigid, non-rigid registration techniques and a particular similarity measurement procedure including three patterns of similarity calculation is described in Chapter 4.

(1) Segmentation of SPNs and blood vessels:
We originally introduce a Hessian and level set-based methodology for the seg-

mentation of both SPNs and vessels. This is the first time for introducing a method that incorporates the enhancement results of Hessian-based LSE and BSE filters into a level set scheme to improve the segmentation performance of both pulmonary nodules and blood vessels. The conventional methods focus on employing only BSE or LSE filter to execute the initial segmentation of nodules or blood vessels. However, due to similar intensity, incorrect discriminations of the nodules and blood vessels may occur in the enhancement results The key-point is how to discriminate the blood vessels and nodules. To deal with such problem, the proposed method incorporated the initial vessel regions and nodule candidates into the level set-based front surface propagation (FSP) procedure, and make the front surface cover only the blood vessels with suppression of nodules by developing a specified speed function. Consequently, both nodules and blood vessels can be finely segmented.

(2) Nodule matching:

This dissertation originally introduces an automatic nodule matching method that can match the nodules with temporal changes such as merger/separation and appearance/disappearance. We consider three patterns of similarity measurement for the matching of normal nodules, merged/separated nodules and appeared/ disappeared nodules, respectively. Also, this method can avoid the incorrect matching of actual nodules and FPs. By utilizing features of average intensity and diameter of nodule for the similarity measure, although two nodule candidates locating close in CT images, they will not be considered as corresponding nodules if there features are totally different. Furthermore, the propose nodule matching method has good performance on compensation of both inelastic and elastic deformations. A roughly global registration, the affine registration, and the non-rigid registration are used for the compensation of such deformations between two CT images.

Chapter 3

Automated segmentations of lung nodules and pulmonary blood vessels from 3D chest CT images

This chapter introduces an automated segmentation method for both solitary pulmonary nodules (SPNs) and pulmonary blood vessels. The proposed method combines Hessian-based BSE, LSE filters and the Level set-based FSP procedure for segmenting nodules and blood vessels finely and separately.

3.1 Purpose

Figure 3.1 summaries the main problems in the segmentation of SPNs and pulmonary blood vessels as well as the solutions in our method. The main purpose of this method is to improve the segmentation accuracy of both SPNs and pulmonary blood vessels by discerning between them, especially the vessel-attached nodules and vessel bifurcation points. For the segmentation of lung nodules, we focus on:

(1) Segmentation of blood vessel-attached nodules.

(2) Reduction of the FPs generated in blood vessel regions.

For the segmentation of pulmonary blood vessels, we focus on:

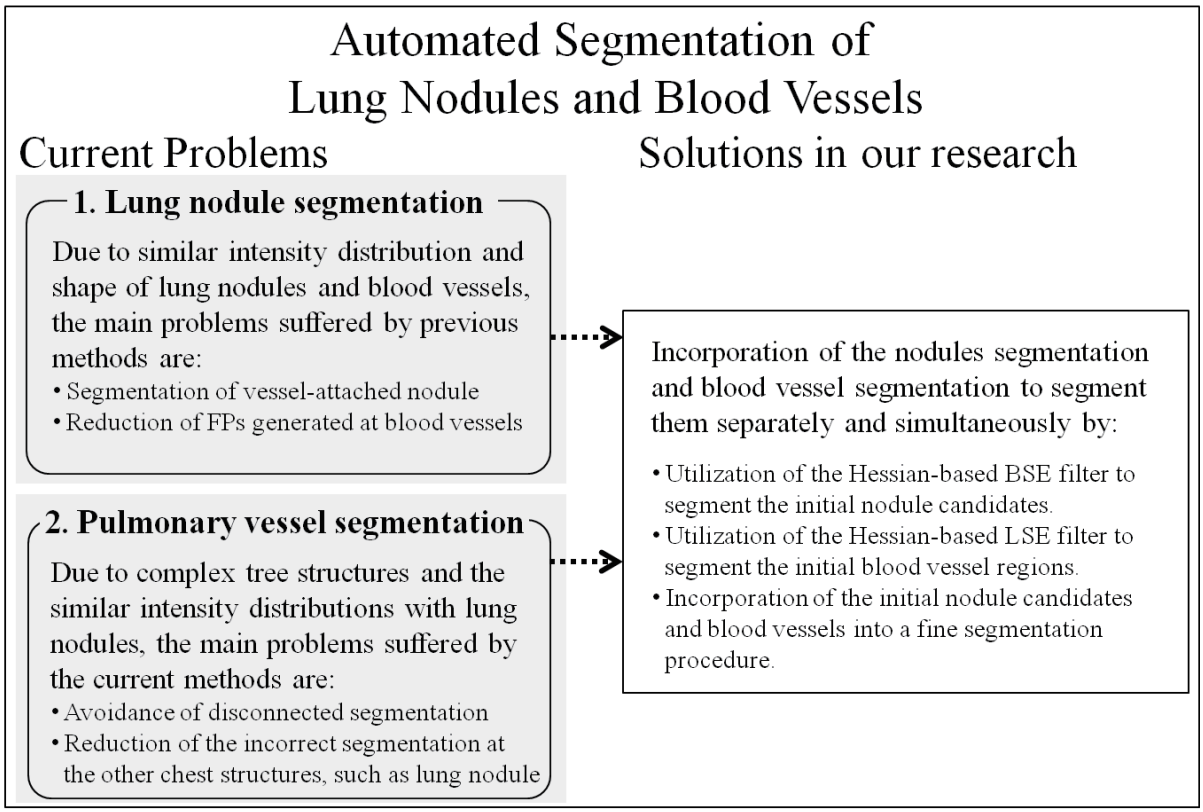

Figure 3.1: The problems in the nodule matching and the solutions of the proposed method

(1) Segmentation of the whole blood vessel trees.

(2) Separation of the blood vessels from the other structures, especially the nodules.

Figure 3.2 shows the volume rendering results of a chest CT image. There are hundreds of SPNs in this patient, including many vessel-attached nodules. Some vessel-attached nodules are marked with white arrows in Fig. 3.2(b). To distinguish such nodules from the blood vessels is challenging. The FPs of a nodule segmentation method are mainly generated in the blood vessel regions, especially the bifurcation points. Figure 3.3 shows examples of a vessel attached nodule (Fig. 3.3 (a)) and a blood vessel bifurcation point (Fig. 3.3 (b)). Since they have very similar features such as shapeand intensity in CT images, reducing the FPs in blood vessels is challenging. Also, obtaining sufficient blood vessel segmentation results, the discrimination of blood vessels and

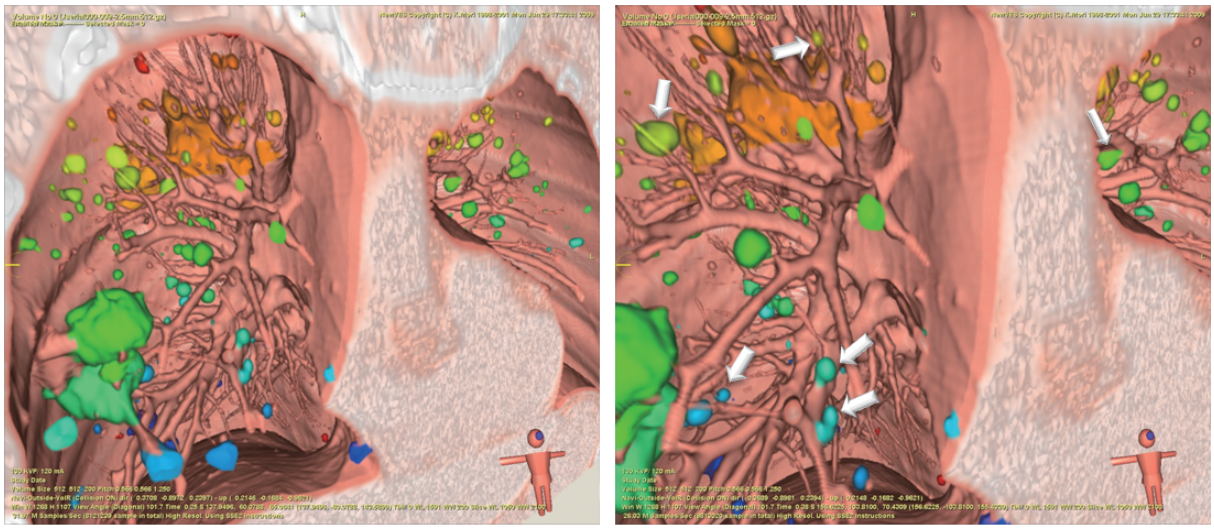

(a) (b)

Figure 3.2: Volume rendering of a chest CT image. There are hundreds of lung nodules generated in the lungs of this patient. We mark the different nodules with different colors. The nodules pointed with white narrows are the vessel-attached ones. To separate such nodules from blood vessels is difficult.

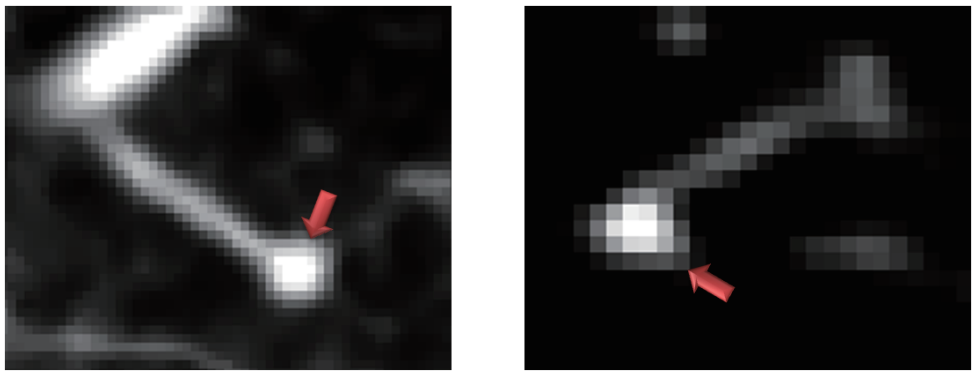

(a) Vessel-attached nodule (b) Vessel bifurcation point

Figure 3.3: Examples of a vessel-attached nodule and blood vessel bifurcation point.

nodules is required.

As shown in Fig. 3.2, in order to handle the above problems and to achieve our purpose, the proposed method segments the initial regions of SPNs and blood vessels by employing Hessian-based BSE, LSE filters, which are confirmed have good performance for enhancing nodular and vascular structures, respectively [47, 80, 113]. Then,

we utilize Level set-based front surface propagation (FSP) procedures to perform fine segmentation. The Level set-based FSP procedure is confirmed as a sufficient tool for the segmentation of vascular structures [133, 134]. We incorporate the initial vessel regions and nodule candidates into the FSP procedure to make the front surface only cover the blood vessels with the suppression of nodules. Consequently, the regions covered by the front surface are considered extracted pulmonary blood vessels, whereas nodule detection results are obtained by removing the nodule candidates covered by the front surface.

Conventional segmentation methods focus on employing only BSE to execute the initial segmentation of nodules. Then, machine learning-based pattern recognition methods are usually utilized for reducing FPs. However, finding reliable features is still difficult, since many blood vessel bifurcations show similar features with nodules (see Fig.4.1). Usually, the incorrect reduction of actual nodules (both attached type and isolated type) is unavoidable due to their unreliable feature selection. The proposed method focus on the elimination of blood vessel regions from nodule candidates to execute FP reduction. This method originally incorporates the enhancement results of LSE and BSE filters into a Level set scheme to improve the segmentation performance of both pulmonary nodules and blood vessels.

3.2 Methods

3.2.1 Overview

Figure 3.4 shows the flowchart of our proposed methods, which consist of three main procedures to segment both the pulmonary blood vessels and the nodules from the input 3D chest CT images: (1) preprocessing that includes the smoothing and extraction of the target processing region, (2) enhancement of the initial blood vessel regions and nodule candidates based on local intensity structure analysis, (3) fine segmentation of the blood vessel trees and nodules by a FSP procedure. Step (3) is the main procedure of the proposed method. We originally introduce a level set-based FSP scheme to propagate

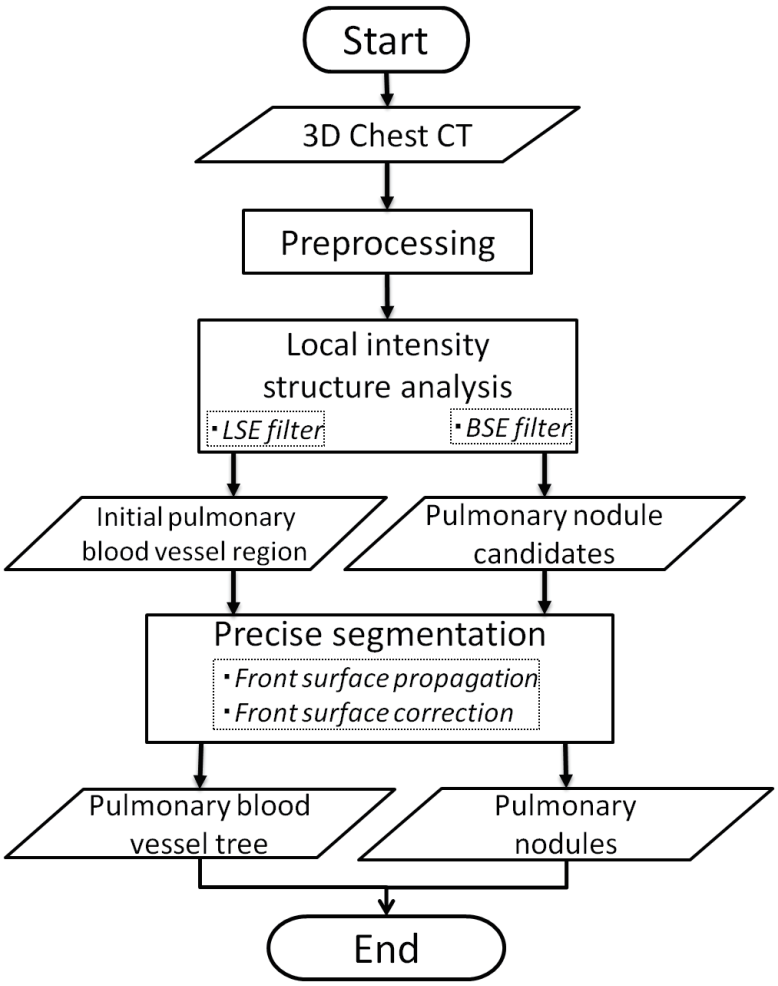

Figure 3.4: Flowchart of the proposed method

the front surface to cover the blood vessel region while suppressing the nodules. When a nodule candidate is covered by the front surface, we consider this candidate a FP and reduce it. However, some bifurcation regions of blood vessels are also suppressed by the propagated front surface because of the incorrect enhancement of the BSE filter. A correction process is performed to modify the front surface to include such bifurcation regions that can significantly improve the segmentation results of both pulmonary blood vessels and nodules. The details of each step are introduced below.

(a) Axial slice of input chest CT image

(a) Segmentation results of target processing region I_{target}

Figure 3.5: Extraction of a processing target region I_{target}. (a) shows an axial slice of a chest CT image. (b) shows the segmentation results of the target processing region I_{target} (blue regions).

3.2.2 Preprocessing

The preprocessing procedure consists of a smoothing process and the segmentation of the target process region. A median filter of a $3 \times 3 \times 3$ voxel mask is utilized to remove the image noise in the input 3D chest CT images. Target processing region I_{target} indicate lung regions without airways, which is the target region for performing the proposed segmentation method. First, we segment the lung regions I_{lung} from smoothed 3D CT images by employing a lung area extraction method that was introduced by Kitasaka et al. [141]. I_{lung} mainly includes pulmonary blood vessels, nodules, and airways. Then I_{target} is obtained by removing airways $I_{airways}$ from I_{lung} (Fig. 3.5). $I_{airways}$ is segmented by performing a region growing-based airway extraction method [142] and a morphological dilation operation that is utilized to approximate the marginal region of the bronchus. The $I_{airways}$ is removed because the bronchus usually runs along the pulmonary blood vessel and is attached to it. Since the intensity contrast between the blood vessels and the marginal regions of bronchus is low, incorrect segmentation of the blood vessels usually occurs at the marginal regions of the bronchus.

3.2.3 Local intensity structures analysis

A pulmonary blood vessel segment usually shows a line-like shape, but an SPN typically shows a blob-like shape on CT images. We enhance the voxels that belong to line and blob structures respectively by investigating the profile computed from a Hessian matrix at every voxel in a local region in I_{target}. The Hessian matrix is computed from second-order partial derivatives, which are highly sensitive to noise. To address noise elimination, Sato et al. [111] introduced 3D multi-scale enhancement filters based on differentiation, which were defined as convolution with derivatives of Gaussians. By adjusting the standard deviation σ of the Gaussian distribution, the enhancement filters can emphasize structures of different sizes. However, Gaussian smoothing usually changes the intensity of vessel bifurcation so that it resembles a blob structure, which leads to incorrect enhancements at such bifurcation regions. The smoothing procedure may also enlarge the target structure [143]. To avoid smoothing, we apply an optimum surface fitting (OSF) that is robust to the image noise instead of Gaussian kernel convolution. In input image $\mathbf{F} = \{f_{i,j,k}\}$, a hypersurface is produced to approximate the CT value on a local region (cubic region whose edge length is h_i) that indicates neighborhoods $N(i,j,k)$ of an interested voxel (i,j,k). A quadratic polynomial of three variables $\phi(x,y,z;\mathbf{a})$

$$\begin{aligned} \phi(x,y,z;\mathbf{a}) &= a_1x^2 + a_2y^2 + a_3z^2 \\ &+ a_4xy + a_5yz + a_6zx + a_7x + a_8y + a_9z + a_{10} \end{aligned} \tag{3.1}$$

is utilized to indicate the hypersurface. $\mathbf{a}$ is a coefficient vector represented as $\mathbf{a} = (a_1, ..., a_{10})$. Then minimum mean square error $\epsilon_{i,j,k}$ between $\mathbf{F}$ and ϕ is given as

$$\epsilon_{i,j,k} = \sum_{p,q,r \in N(i,j,k)} \{f_{i,j,k} - \phi(p,q,r;\mathbf{a})\}^2, \tag{3.2}$$

where (p,q,r) indicates the coordinate of a voxel in local region $N(i,j,k)$. $f_{i,j,k}$ indicates the CT value at (i,j,k). Thus, optimum $\mathbf{a}$ that minimizes $\epsilon_{i,j,k}$ can be obtained by solving

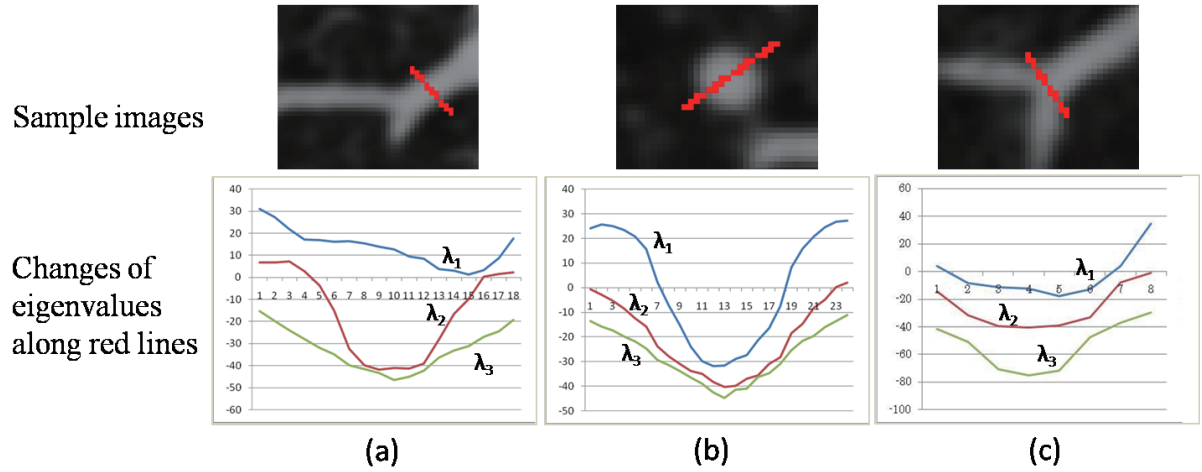

Figure 3.6: Eigenvalue distribution of the Hessian matrix during local intensity structure analysis [145]. (a) shows eigenvalues of the Hessian matrix on a branch of blood vessels, (b) shows eigenvalues of a Hessian matrix on a nodule and (c) shows eigenvalues on a vessel bifurcation.

the following simultaneous functions:

$$\frac{\partial \epsilon_{i,j,k}}{\partial a_m} = -2\frac{\partial \phi}{\partial a_m} \sum_{p,q,r \in N(i,j,k)} \{f_{i,j,k} - \phi(p,q,r;\mathbf{a})\} = 0, \tag{3.3}$$

where $m = 1, 2, ..., 10$. Then, a Hessian matrix **H** is obtained by consisting of second-order partial differential coefficients of ϕ at (i, j, k), shown as

$$\mathbf{H} = \begin{bmatrix} \frac{\partial^2\phi}{\partial x^2}|_{(i,j,k)} & \frac{\partial^2\phi}{\partial x\partial y}|_{(i,j,k)} & \frac{\partial^2\phi}{\partial x\partial z}|_{(i,j,k)} \\ \frac{\partial^2\phi}{\partial y\partial x}|_{(i,j,k)} & \frac{\partial^2\phi}{\partial y^2}|_{(i,j,k)} & \frac{\partial^2\phi}{\partial y\partial z}|_{(i,j,k)} \\ \frac{\partial^2\phi}{\partial z\partial x}|_{(i,j,k)} & \frac{\partial^2\phi}{\partial z\partial y}|_{(i,j,k)} & \frac{\partial^2\phi}{\partial z^2}|_{(i,j,k)} \end{bmatrix}. \tag{3.4}$$

If the eigenvalues of **H** at voxel (i, j, k) satisfy the condition of $\lambda_3 \cong \lambda_2 \ll \lambda_1 \cong 0$, then this voxel generally belongs to a line structure such as blood vessel segment (Fig. 3.6(a)). Following this feature, Krissian et al. [138] proposed a model-based detection method of tubular structures, which defined a vessel detector by combining the two highest eigenvalues (λ_1, λ_2). Sato et al. [110, 111] proposed a LSE filter that incorporates all three eigenvalues as

$$S_{line}(i,j,k) = \begin{cases} \mid \lambda_3 \mid \cdot\psi(\lambda_2;\lambda_3)\cdot\omega(\lambda_1;\lambda_2), & \lambda_3 \leq \lambda_2 < 0 \\ 0, & \text{otherwise} \end{cases} \tag{3.5}$$

where $\mid \lambda_3 \mid$ is utilized to control the magnitude of S_{line}. $\psi(\lambda_2;\lambda_3)$ and $\omega(\lambda_1;\lambda_2)$ are weight functions written as

$$\psi(\lambda_2;\lambda_3) = \begin{cases} (\frac{\lambda_2}{\lambda_3})^{\mu}, & if\ \lambda_3 \leq \lambda_2 < 0 \\ 0, & \text{otherwise} \end{cases} \tag{3.6}$$

and

$$\omega(\lambda_1;\lambda_2) = \begin{cases} (1+\frac{\lambda_1}{|\lambda_2|})^{\mu}, & if\ \lambda_2 \leq \lambda_1 < 0 \\ (1-\alpha\frac{\lambda_1}{|\lambda_2|})^{\mu}, & if\ \frac{|\lambda_2|}{\alpha} > \lambda_1 > 0 \\ 0, & \text{otherwise} \end{cases} \tag{3.7}$$

μ and α are parameters, $\psi(\lambda_2;\lambda_3)$ differentiates line-like structure from sheet-like structure. $\omega(\lambda_1;\lambda_2)$ differentiates line-like structures from both sheet-like and blob-like structures, since its output value is close to 1 only at line-like structure. The output value of $S_{line}(i,j,k)$ shows the likelihood of the lineness of voxel (i,j,k). Frangi et al. introduced a similar LSE filter [136], and Descoteaux et al. incorporated this filter into a geometric flow for segmenting vasculature [137].

However, the eigenvalues at vessel bifurcation points show the relation of $\lambda_3 < \lambda_2 < \lambda_1 \approx 0$ (Fig. 3.6(c))[145], the above conventional LSE filters may output low values that are close to the one at a nodule. This usually causes the discontinuity of the blood vessel tree at a bifurcation. To separate vessel bifurcations and nodules, we modified the LSE filter in Eq. (3.5) as

$$LSE(i,j,k) = \begin{cases} \mid \lambda_3/\left(\lambda_1+1\right) \mid \cdot\psi(\lambda_2;\lambda_3)\cdot\omega(\lambda_1;\lambda_2), & \\ \qquad\qquad \lambda_3 \leq \lambda_2 < 0 & \\ 0, \qquad \text{otherwise}. & \end{cases} \tag{3.8}$$

Since the absolute value of λ_1 at both the line-like structure and the bifurcation point is much lower than the absolute value of λ_3; that at a blob structure is closer to the absolute value of λ_3, this new LSE filter outputs higher enhancement values at vessel

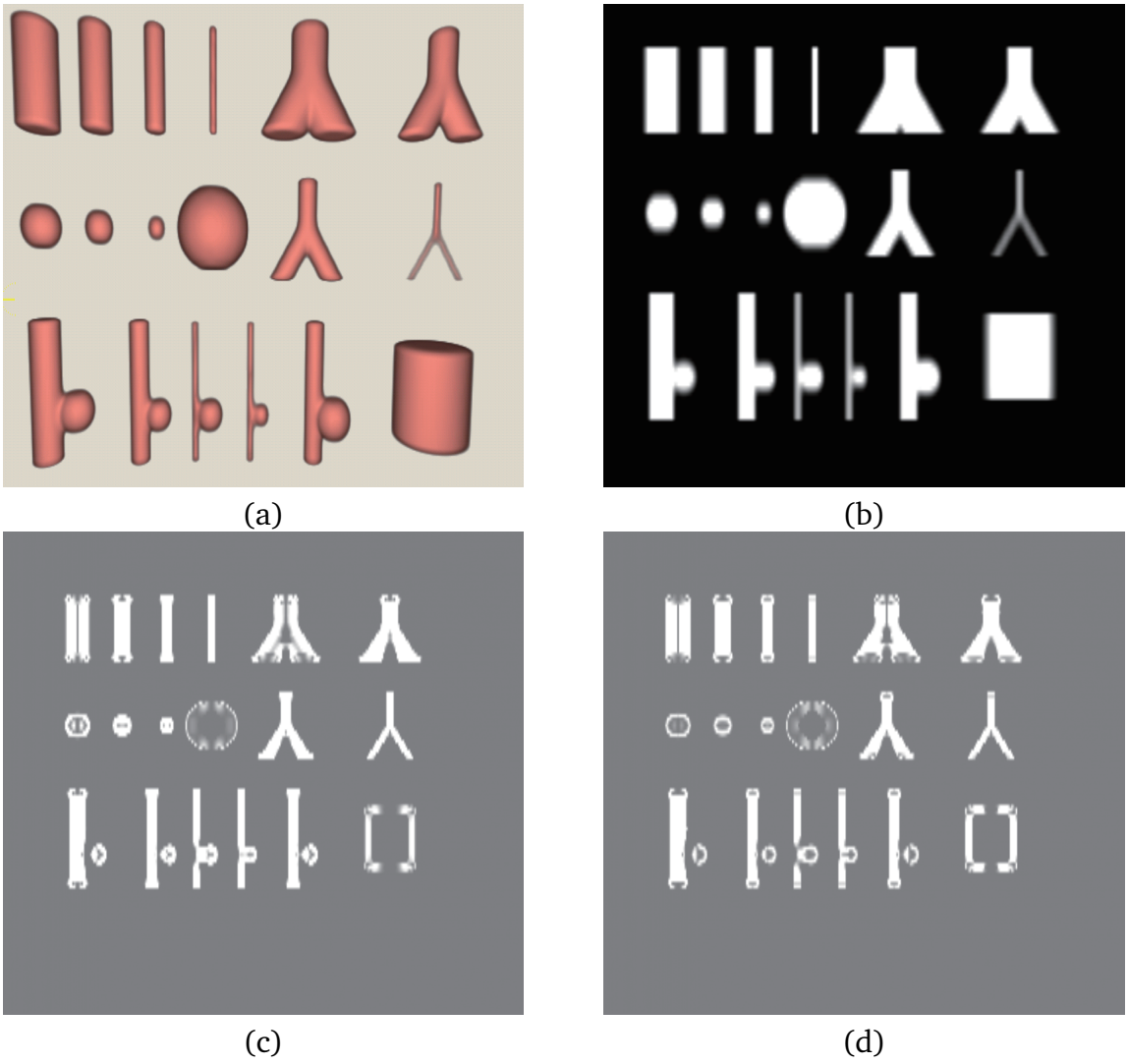

(a) (b)

(c) (d)

Figure 3.7: Results of line structure enhancement filters. (a) The volume of the original synthetic image (b) One slice of the original synthetic images, (c) The result of previous LSE filter [111] and (d) The result of the newly proposed LSE filter.

bifurcations than the value at the nodules. Figure 3.7 shows the comparison results of performing this new LSE filter and the previous one introduced in Eq. (3.5) to an artificial image, which includes various sizes of line structures, blob structures, junction structures, and blob structures attached to line structures. The results show that the proposed LSE filter outputs a relatively-lower value (Fig. 3.7(d)) at the blob structure (especially at the center region) than the previous one (Fig. 3.7(c)).

If the eigenvalues of a voxel satisfy the conditions of $\lambda_3 \cong \lambda_2 \cong \lambda_1 \ll 0$, generally,

this voxel belongs to a blob structure such as nodules (Fig. 3.6 (b)). Following this feature, Sato et al. [111] and Li et al. [80] introduced two BSE filters using $\mid \lambda_3 \mid$ as the magnitude function of the output value. Oda et al. [144] proposed another BSE filter that used $\mid \lambda_1 \mid$ as the magnitude function of output value as

$$BSE(i,j,k) = \begin{cases} \frac{(\lambda_1)^2}{\hat{\lambda}}, & if\ 0 > \lambda_1, \lambda_2, \lambda_3, \\ 0, & \text{otherwise} \end{cases} \tag{3.9}$$

where $\hat{\lambda} = \mid \lambda_1 + \lambda_2 + \lambda_3 \mid /3$. BSE filter in Eq. 3.9 only outputs high values in the case of [$\lambda_1 \ll 0$ and $\lambda_1 \approx \hat{\lambda}$]. Therefore they can be utilized to enhance blob-like structures. The output value of BSE(i,j,k) indicates the likelihood of the blobness of voxel (i,j,k). The use of $\mid \lambda_1 \mid$ prevents the false enhancement of structures [144], such as blood vessels. In this paper, we utilized the BSE filter shown in Eq. 3.9 to enhance the blob-like structures in input CT image.

We utilize both the new LSE and BSE filters across multiple scales as

$$MS\_LSE(i,j,k) = \max_{r_i} \gamma LSE_{r_i}(i,j,k) \tag{3.10}$$

and

$$MS\_BSE(i,j,k) = \max_{r_i} \gamma BSE_{r_i}(i,j,k) \tag{3.11}$$

to enhance the blood vessels and nodules of different sizes. We assume that the radius of the local region $(h_i/2mm)$ corresponds to the radius of the objective structure, the scale r_i is set to $h_i/2$. Therefore, the calculation of the enhancement filter across multiple scales is equivalent to calculating the Hessian matrix on different sizes of local regions. Parameter γ is a normalization coefficient, which is utilized to control the average enhancement response of multiple scales. $LSE_{r_i}(i,j,k)$ and $BSE_{r_i}(i,j,k)$ indicate the filter output values at voxel (i,j,k) when the scale is r_i. When voxel (i,j,k) obtains the maximum enhancement value at the r_i scale, this scale must be the optimum scale for it.

We apply $MS\_LSE(i,j,k)$ and $MS\_BSE(i,j,k)$ filters to the voxels in I_{target} whose

CT values range from V_l to V_h. Initial pulmonary blood vessels I_{lse} and nodule candidates I_{bse} are obtained as the region whose enhancement value of $MS\_LSE(i,j,k)$ or $MS\_BSE(i,j,k)$ is larger than 0. Due to the similar intensity of the blood vessels and the nodules, the incorrect enhancement of both MS_LSE and MS_BSE filters may occur. This causes the initial pulmonary blood vessels I_{lse} to be discontinued and includes non-vessel regions such as nodules, while nodule candidates I_{bse} may include many FPs that are mainly produced at the blood vessels.

3.2.4 Fine segmentation of pulmonary blood vessel and nodules

3.2.4.1 Front surface propagation (FSP)

We utilize an FSP procedure based on FMM [98] to perform fine segmentation. FMM is a numerical technique for tracking the interfaces and shapes, which extended from $level-sets$. FMM propagates an initial front surface (Γ) outwards with speed function $V(i,j,k) > 0$ that depends on the image itself. Thus, FMM can describe the evolution of the front surface as a function of arrival time $T(i,j,k)$ at voxel point (i,j,k) on the surface as

$$\mid \nabla T \mid V = 1, \quad T = 0 \; on \; \Gamma. \tag{3.12}$$

The front surface is propagated based on arrival time $T(i,j,k)$. The FMM procedure can segment a desired object by defining an initial front surface inside it and constructing a speed function that follows its features.

We segment the pulmonary blood vessel trees with suppressed nodule extraction by incorporating initial segmentation results I_{lse} and I_{bse} into the FMM scheme. A region inside the pulmonary blood vessel is defined as the initial front surface. Then we construct a speed function that becomes fast at initial pulmonary blood vessels I_{lse} and slow at nodule candidates I_{bse} to propagate the front surface. Consequently, the regions covered by the front surface can be considered segmented pulmonary blood vessels. The nodule segmentation result is obtained by removing the nodule candidates covered by

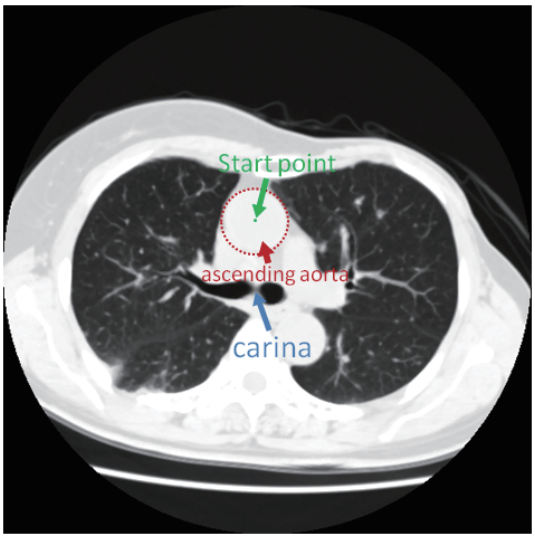

(a) Slice containing the carina

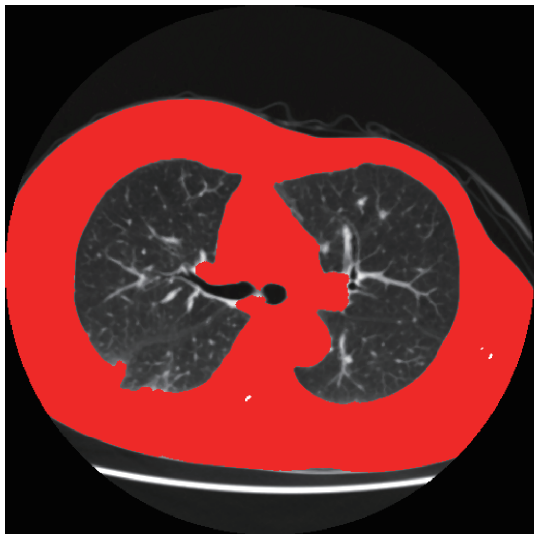

(b) Region of I_1

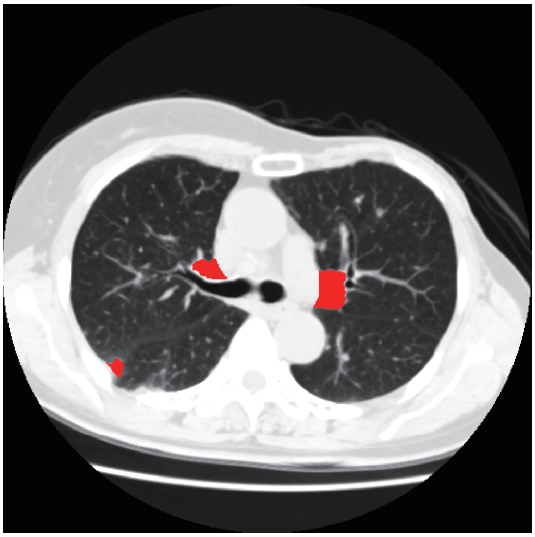

(c) Region of I_2

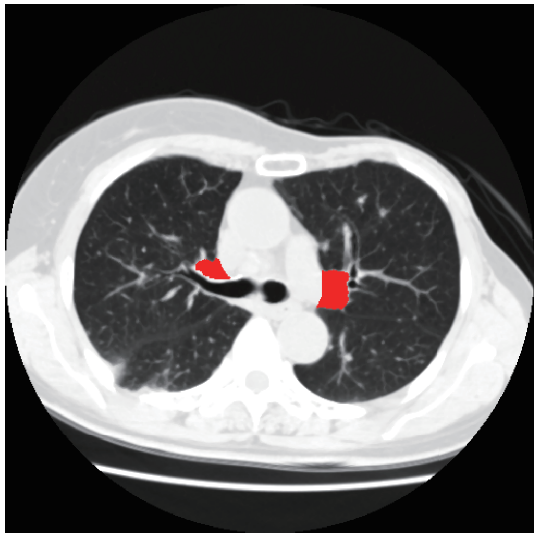

(d) Region of I_{hilar}

Figure 3.8: Segmentation of initial front surface I_{hilar}. (a) shows an axial slice of a chest CT image that contains a carina. The starting point of the region growing is the centerline point of ascending aorta, (b) shows the segmentation results of region I_1, (c) shows region I_2 and (d) shows region I_{thick} utilized as the initial front surface.

the front surface.

3.2.4.2 Initialization of front surface

We segment the thick vessel near the lung hilar (I_{hilar}) as the initial front surface of the FMM. The segmentation of I_{hilar} consists of three procedures. First, we utilize a

region growing method with a spherical structure element whose radius is $5\ [mm]$ to segment region I_1 (Fig. 3.8(b)). The starting point of the region growing is selected as the centerline point of the ascending aorta on the axial slice, which contains the carina (Fig. 3.8(a)). The approach for finding this centerline point is introduced by Feuerstein et al. [140]. Second, a logical disjunction process is performed between I_1 and I_{target} to get region I_2 (Fig. 3.8(c)), contains I_{hilar} and some chest wall-attached nodules. Third, we select the largest connected component from the right and left lung regions as the I_{hilar} region (Fig. 3.8(d)).

3.2.4.3 Construction of speed function

We utilize the following speed function,

$$F(i,j,k) = F_{line\_blob}(i,j,k) \times F_{margin}(i,j,k), \tag{3.13}$$

to propagate the front surface. $F(i,j,k)$ represents the propagation speed at voxel (i,j,k). In Eq. (3.13), function $F_{line\_blob}\ (i,j,k)$ shows a speed that is based on the likelihood of *lineness* and *blobness* at voxel (i,j,k). $F_{line\_blob}(i,j,k)$ is constructed by incorporating initial blood vessels I_{lse} and nodule candidates I_{bse} as

$$F_{line\_blob} = e^{t_1 \cdot f(i,j,k)}, \tag{3.14}$$

where

$$f(i,j,k) = L(i,j,k) - \kappa B(i,j,k) \tag{3.15}$$

t_1 is a parameter that is utilized to normalize the value of $f(i,j,k)$. $L(i,j,k)$ denotes the enhancement value of the *MS_LSE* filter, and $B(i,j,k)$ denotes the enhancement value of MS_BSE at voxel (i,j,k). κ is a normalization coefficient that is defined as $\kappa = \hat{L}/\hat{B}$, where $\hat{L}$ and $\hat{B}$ are the average enhancement values of the voxels belonging to I_{lse} and I_{bse}, respectively. The function $f(i,j,k)$ combines the output values of *MS_LSE* and *MS_BSE* filters at a voxel (i,j,k). Although this voxel may be enhanced by both *MS_LSE* and *MS_BSE* filters, f generally outputs a large value at the line-like region,

while outputing low values at the blob-like region. Hence, F_{line_blob} is configured to perform fast propagation on line-like regions and slow propagation on blob-like regions, enabling the front surface to cover the blood vessels by suppressing the coverage on the nodules. Function F_{margin}, which is introduced to terminate the propagation at the marginal regions of the blood vesselsand is represented as

$$F_{margin}(i,j,k) = e^{(-t_2 \cdot |\nabla I(i,j,k)|)}, \tag{3.16}$$

where $\nabla I(i,j,k)$ denotes the $gradient$ at voxel (i,j,k). A parameter t_2 is utilized to normalize the value of $\nabla I(i,j,k)$. The intensity around the centerline of the blood vessel changes slowly but decreases rapidly near the marginal regions in CT images. By investigating the $\nabla I(i,j,k)$ of each voxel, we construct function F_{margin} to output small values around the marginal region so that the surface propagation can be terminated. The front surface is propagated by speed function $F(i,j,k)$ to perform the fine segmentation of the pulmonary blood vessels and nodules. We consider that the region covered by the front surface belongs to the blood vessel region. When a nodule candidate in I_{bse} is covered by the front surface, this is an FP of nodule detection, and we remove it from the nodule candidates.

3.2.4.4 Correction of front surface

However, some vessel bifurcations show similar intensity distributions to a nodule, which lead to the incorrect enhancement of the MS_BSE filter at such bifurcations. These bifurcations may also be enhanced by the MS_LSE filter since they are part of the blood vessels. Whether front surface propagation terminates at such regions depends on the enhancement values of the MS_LSE and MS_BSE filters. The incorrect termination of propagation occurs when MS_BSE outputs much higher enhancement values. A correction procedure of front surface is required to reduce such incorrect termination.

Due to the incorporation of I_{lse} and I_{bse}, the incorrectly terminated front surface usually shows an irregular shape and the voxels around it show a high rate of blood

vessels (A(i) in Fig. 3.9). The front surface that is correctly terminated at an actual nodule usually shows a regular sphere shape and only a few voxels around it belong to blood vessels (B(i) in Fig. 3.9). Following such features as *shape* and *neighborhood profile*, we perform *nodule checking processing* to check the terminated front surface and modify the incorrectly terminated one. The details of this *nodule checking processing* are described below.

Nodule checking processing

Input: Terminated front surfaces

Output: Modified front surfaces

Procedure:

1. Select all terminated front surfaces $S_i(i = 1, 2, ..., m)$ that stop at the nodule candidates (A(ii) and B(ii) in Fig. 3.9). m is the number of selected front surfaces.

2. Extract volume region B_i, which consists of connected voxels that are surrounded by S_i and belong to the nodule candidates in I_{bse} (A(iii) and B(iii) in Fig. 3.9). The extraction process is performed by executing a region growing scheme

3. Calculate centroid G of each B_i (A(iii) and B(iii) in Fig. 3.9). Search for B_i whose centroid G is outside of it or whose intensity of G is lower than the average intensity. Consider such B_i a non-nodule and eliminate its corresponding nodule candidate from I_{bse}.

4. Apply a *neighborhood profile* checking procedure to the remaining B_i, which means calculating the ratio of the blood vessel voxels in spherical region Ω around each remaining B_i. From Fig. 3.6(b), we find that the eigenvalues of the Hessian matrix around the marginal region of nodules become line-likely, so the output value of the MS_BSE filter at such region becomes low and the front surfaces usually cover such regions incorrectly (Fig. 3.9(B(i))). To avoid such regions, spherical

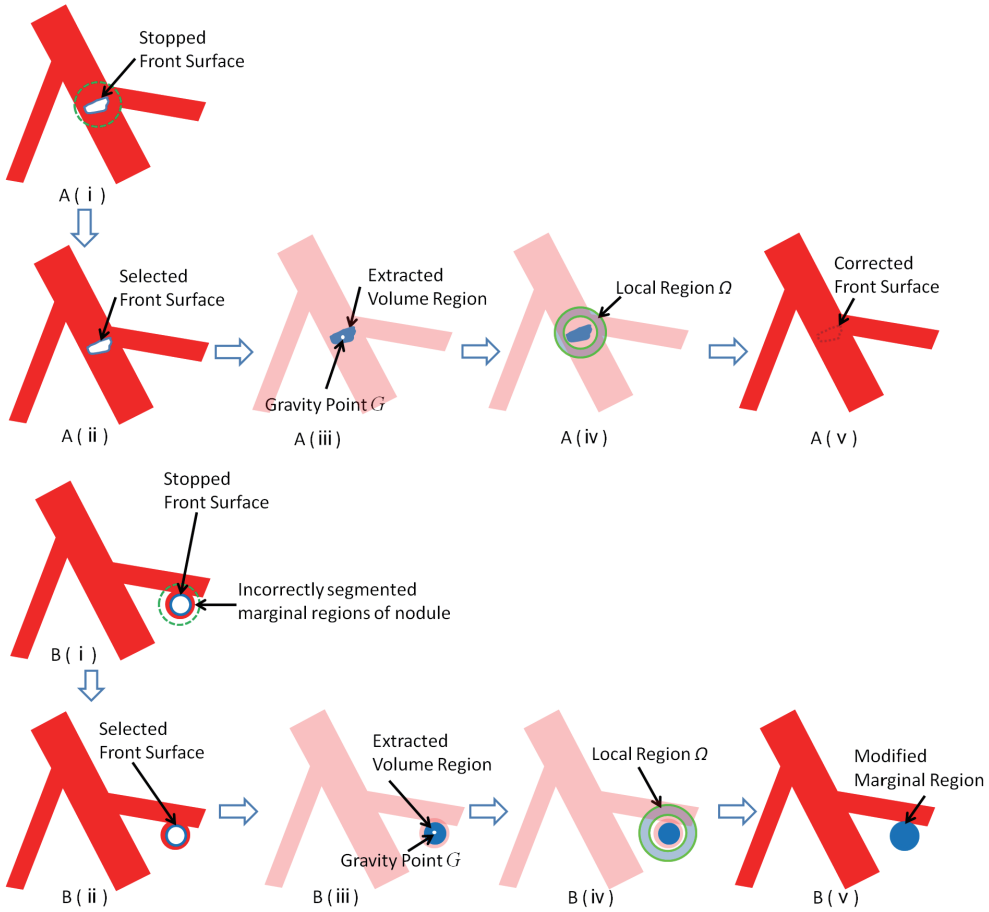

Figure 3.9: Illustration of *nodule checking processing*. Front surface that terminates at blood vessel regions usually shows an irregular shape (A(i) in Fig. 3.9), whereas the one terminated at nodules shows a regular spherical shape (B(i) in Fig. 3.9). During *nodule checking processing*, we first select whole front surfaces S_i that stopped at nodule candidates (A(ii) and B(ii) in Fig. 3.9).Volume region of B_i is extracted using region growing from S_i, and the centroid G of B_i is found (A(iii) and B(iii) in Fig. 3.9). Add each B_i that is considered a non-nodule into front surface (Fig. 3.9(A(v)). For that considered a nodule, restore the nodule candidates that correspond to B_i (B(v) in Fig. 3.9).

region Ω is located between $2r$ and $3r$ from G of each B_i ((A(iv)) and B(iv) in Fig. 3.9), and r is the radius of B_i.

5. Consider B_i, whose ratio of vessel region inside Ω is larger than ρ, a non-nodule, and eliminate the corresponding nodule candidate of such B_i from I_{bse}. Consider B_i whose ratio of vessel region inside Ω is lower than ρ, an actual nodule, and

Table 3.1: Acquisition Parameters of chest CT images

	Dataset 1	Dataset 2
Image size (voxels)	512×512	512×512
Number of slices	$185 - 728$	$103 - 350$
Pixel spacing (mm)	$0.523 - 0.684$	$0.508 - 0.762$
Slice spacing (mm)	1.25	$1.25 - 2.5$
Slice thickness (mm)	2.5	$1.25 - 2.5$
Tube voltage (kV)	$120 - 140$	$120 - 140$
Tube current (mA)	$100 - 320$	$30 - 75$

modify its marginal regions (Fig. 3.9(B(v))).

6. Add each B_i that is recognized as a non-nodule to the blood vessels (Fig. 3.9(A(v))). Restart the propagation by the modified front surface.

The procedure described above is applied iteratively until no new modification of the front surface occurs.

3.2.4.5 Final segmentation

We obtain the final segmentation results after the *nodule checking processing* is stopped. The regions covered by the front surface are considered the final segmentation results of the pulmonary blood vessel. The modified nodules are considered the final nodule regions.

3.3 Experiments

The performance of the proposed method was evaluated by comparing the results with the ground truth data of both the nodules and the blood vessels. To verify the effectiveness of the OSF procedure for local intensity analysis, we compared the performance of the proposed method (OSF+FSP) to that of the Gaussian kernel convolution (GKC)-based method (GKC+FSP) on the same datasets. To verify the effectiveness of the proposed method on the segmentation of the pulmonary blood vessel, we compared it

to a blood vessel segmentation method based on the MS_LSE filter and region growing (LSE+RG). We also compared the performance of the proposed method to a nodule detection method based on the MS_BSE filter and the reduction of a small connecting component (BSE+RSCC) to verify the effectiveness of the proposed method on the segmentation of the pulmonary nodules.

The proposed method was applied to two datasets of 3D chest CT images. The first dataset includes 20 cases of standard-dose CT images that were randomly chosen from our local database. The second dataset includes 20 cases of low-dose CT images that were randomly chosen from a public database: LIDC. The specifications of these CT images are shown in Table 3.1. We used the first dataset for determining the parameters of our proposed method and validation for the segmentation of both pulmonary SPNs and blood vessels. The second dataset is only used for validating the segmentation of SPNs by using determined parameters. A total of 416 and 55 SPNs with diameters from about 3.0 mm to 27 mm were manually identified by physicians from these two datasets. To verify the performance of the proposed method on pulmonary blood vessels segmentation in terms of the sensitivity of segmented vessels, we manually segmented 10 sets of pulmonary blood vessels (validated by physicians) from dataset 1 as the ground truth. To obtain the ground truth data of the whole datasets is extremely exhausting and time consuming.

While testing the proposed method on dataset 1, we set the range of CT values in the local intensity analysis as $V_l = -700$ H.U., $V_h = 400$ H.U. (mentioned in Section 3.2.3), since most of the blood vessels and nodules can be observed among this intensity range on standard-dose CT images. We set the parameters α and μ to 0.25 and 0.5, as suggested in Sato et al. ([111]). The threshold T_{stop} and ρ were set to 15000 and 0.3, which was determined experimentally (we discuss them in Sections 3.4.1 and 3.4.2). To determine the normalization coefficient γ of MS_LSE and MS_BSE filters, we applied the unnormalized filters to the CT images in dataset 1. Multiple scales were set as [1.25, 2.5, ... 10 mm]. The blue curves in Fig. 3.10 show the average responses of the unnormalized filters, the one in Fig. 3.10(a) was approximated to

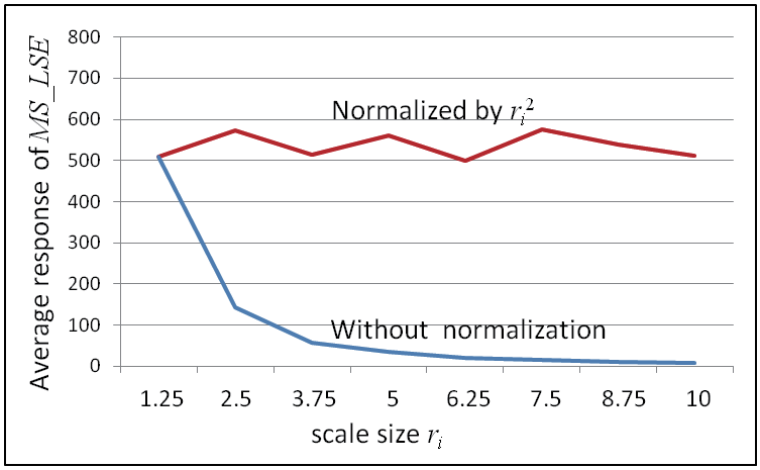

(a) Normalization factor γ of MS_LSE filter

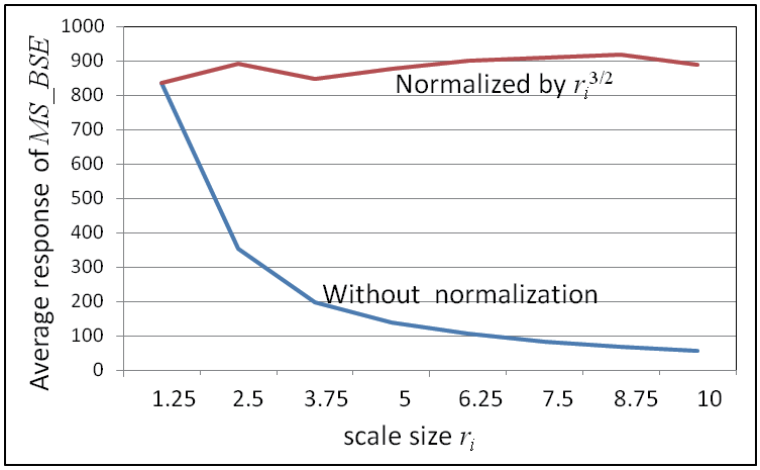

(b) Normalization factor γ of MS_BSE filter

Figure 3.10: Average response of MS_LSE and MS_BSE filters. Blue curves show the average response without normalization on single scale arranged 1.0 mm to 8.0 mm with step of 1.0 mm, and red ones show the curve by normalization. Normalization factor γ of MS_LSE and MS_BSE filters is r_i^2 and $r_i^{3/2}$, respectively.

$y = 530x^2$, and the one in Fig. 3.10(b) was approximated to $y = 843x^{1.5}$ by curve fitting. Hence, we set the normalization coefficient γ of the MS_LSE and MS_BSE filters to r_i^2 and $r_i^{3/2}$, respectively. The red curves in Fig. 3.10 denotes the average enhancement responses of the normalized MS_LSE and MS_BSE filters. To verify our assumption that the scale (radius of local region: $h/2$ mm) corresponds with the radius of objective structure, we investigated the average responses of BSE and LSE filters at the center of the structures in Fig. 3.7. The results are shown in Fig. 3.11.

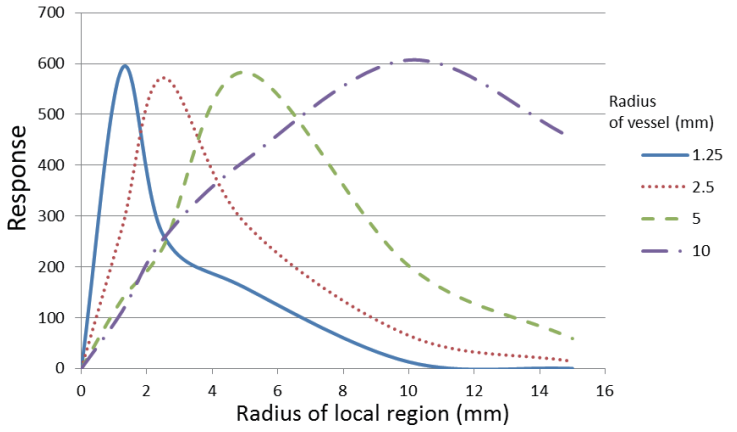

(a)

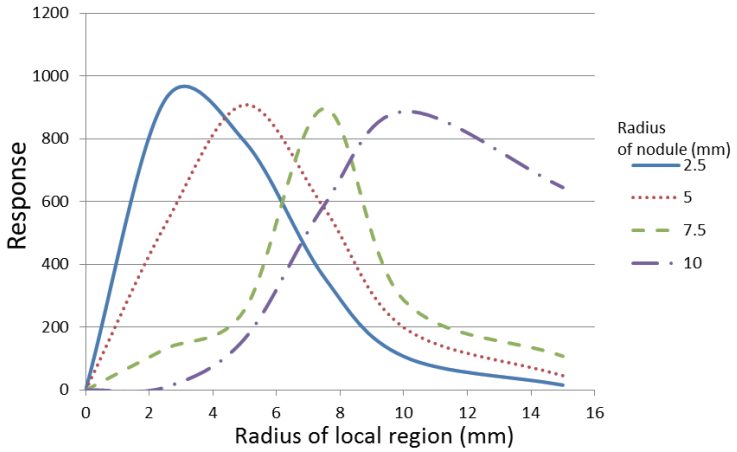

(b)

Figure 3.11: Illustration of normalized responses of LSE and BSE filters on different scales (the radius of local region) at the center of different structures in Fig. 3.7. The largest responses of both BSE and LSE filters are obtained when the scale is approximate to the radius of objective structures. (a) shows the responses of LSE filter at line structures with different radii $(1.25, 2.5, 5, 10mm)$, and (b) shows the responses of the BSE filter at blob structures with different radii $(2.5, 5, 7.5, 10mm)$.

The responses of both BSE and LSE filters obtain the largest values while the radius of the local region approximates to the radius of structure, which confirmed that our assumption was correct. Hence, the configuration of multiple scales depends on the size of the enhancement target. In our experiments, the smallest scale and interval were set equivalent to the slice spacing $(1.25$ mm) of the input CT images in dataset 1. We segmented the blood vessels of diameter less than 12 mm, since usually no vessel

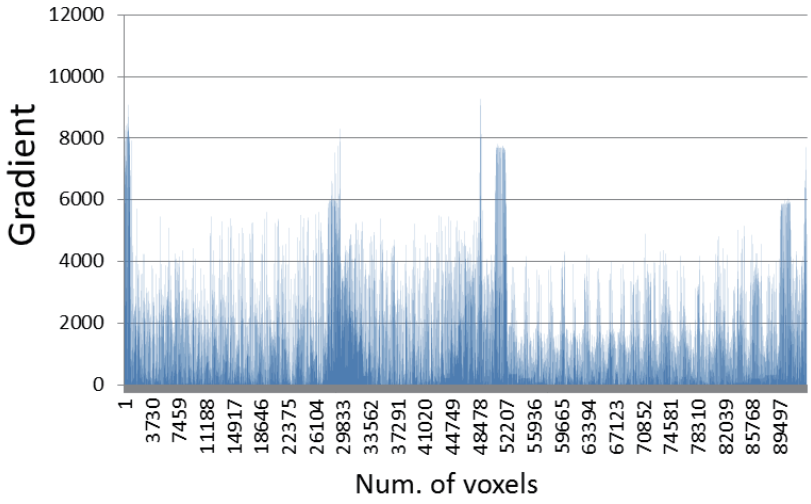

Figure 3.12: An example of gradient distribution calculated from one CT image.

has a larger diameter except for the thick vessels near the hilar, which are extracted as the initial front surface in the fine segmentation procedure. Thus, we set the multiple scales of MS_LSE as [1.25, 2.5, ... 6.25 mm]. In order to enhance the nodules of the diameters from about 3.0 to 30 mm, multiple scales of MS_BSE were set as [1.25, 2.5, ... 15 mm]. According to Fig. 3.10, the largest output value of filters is close to 1000. To normalize the output value of Eq. (3.15) between 0 and 100, we set the parameter t_1 (in Eq. (3.14)) as $t_1 = 10^{-1}$. Figure 3.12 shows the gradient $\nabla I(i, j, k)$ that is calculated from the input CT image, which shows the largest value is close to 10000. In order to normalize the output value of Eq. ((3.16)), we set the normalization parameter t_2 (in Eq. (3.16)) to $t_2 = 10^{-3}$. After the experiments by using dataset 1, we tested the proposed method with determined parameters by using dataset 2. For each input low-dose CT image, we interpolated its slice spacing to 1.25 mm by using B-spline interpolation. Due to the lower intensity, the lower threshold of intensity value V_l was set to -800 H.U..

The performance of the proposed method was evaluated by comparing the results with the ground truth data of both the nodules and the blood vessels. To verify the effectiveness of the OSF procedure for local intensity analysis, we compared the perfor-

Table 3.2: Pulmonary blood vessel segmentation results of 10 CT images using proposed method

Case	1	2	3	4	5	6	7	8	9	10	Avg.
Num. of branches	1756	1869	1964	1895	2125	2046	1896	2154	2216	1562	1692
Extraction rate (%)	95.9	96.0	94.7	93.7	96.2	91.7	89.7	88.9	87.9	95.3	93.0

mance of the proposed method (OSF+FSP) to that of the Gaussian kernel convolution (GKC)-based method (GKC+FSP) on the same datasets. To verify the effectiveness of the proposed method on the segmentation of the pulmonary blood vessel, we compared it to a blood vessel segmentation method based on the MS_LSE filter and region growing method (LSE+RG). We also compared the performance of the proposed method to a nodule detection method based on the MS_BSE filter and the reduction of a small connecting component (BSE+RSCC) to verify the effectiveness of the proposed method on the segmentation of the pulmonary nodules.

3.4 Results

3.4.1 Validation of pulmonary blood vessel segmentation

We evaluated the performance of the proposed method on pulmonary blood vessel segmentation by ten CT images obtained from dataset 1. We evaluated the extraction rate by the number of vessel branches. The centerline voxels of the ground truth data were detected and used to construct a tree structure of the true pulmonary blood vessels. For each blood vessel branch, if its centerline voxels of ground truth were covered by segmented blood vessels larger than 80%, we considered this branch to be successfully extracted. The different setting of T_{stop} brings different segmentation results of both blood vessels and SPNs. Figure 3.13 shows the iterations of the FSP procedure with different settings of T_{stop} on a CT image. The regions of blood vessel are shown in red,

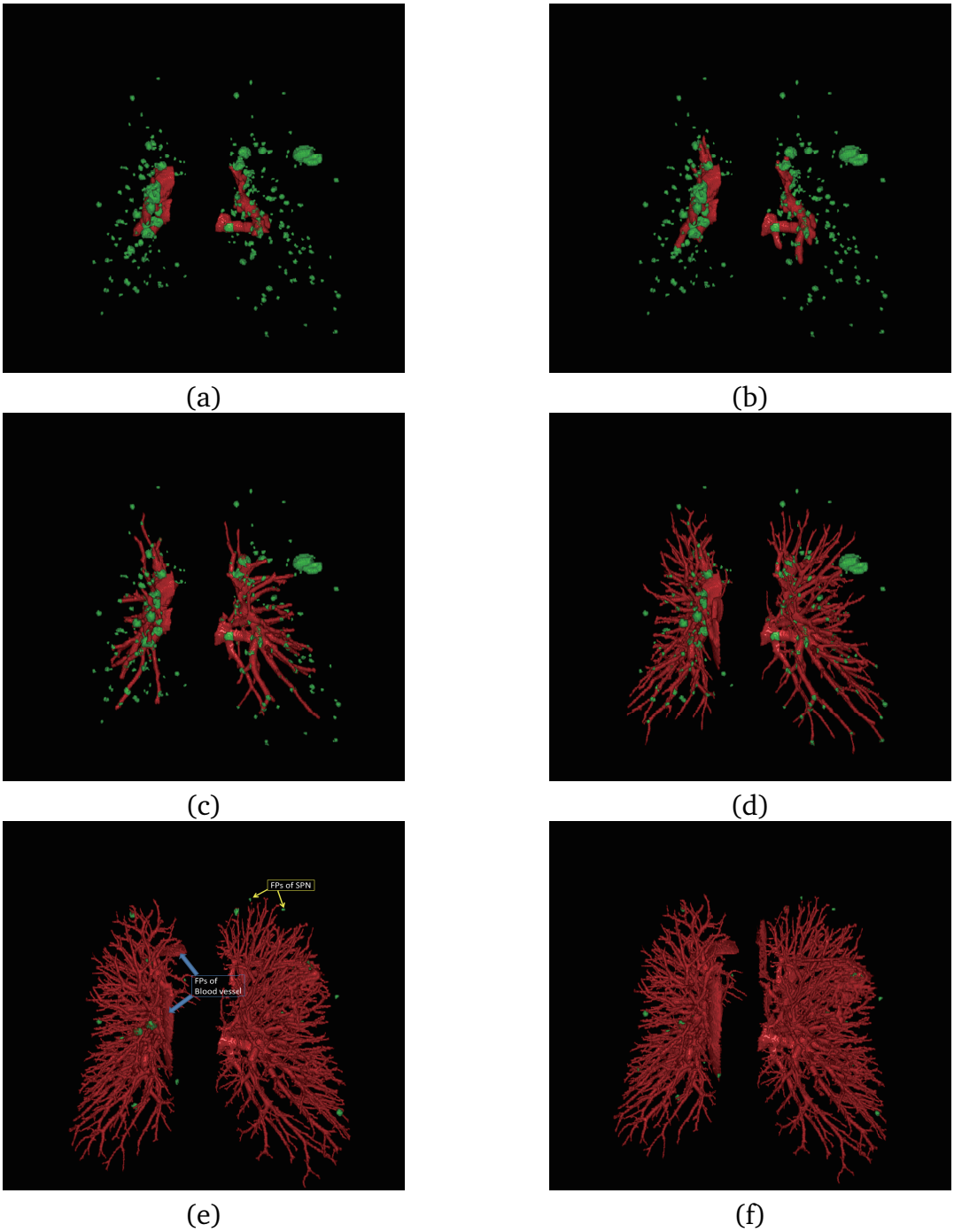

Figure 3.13: Illustration of the iterations of the FSP procedure with different settings of T_{stop} , while (a) T_{stop} = 0, (b) T_{stop} = 10, (c) T_{stop} = 100, (d) T_{stop} = 1500, (e) T_{stop}=15000, and (d) T_{stop}=20000. The regions of blood vessel are shown in red, and the candidates of SPNs are shown in green. With the growing of T_{stop}, the regions of the blood vessel are propagated and the FPs of SPNs are reduced. (e) shows the final segmentation result.

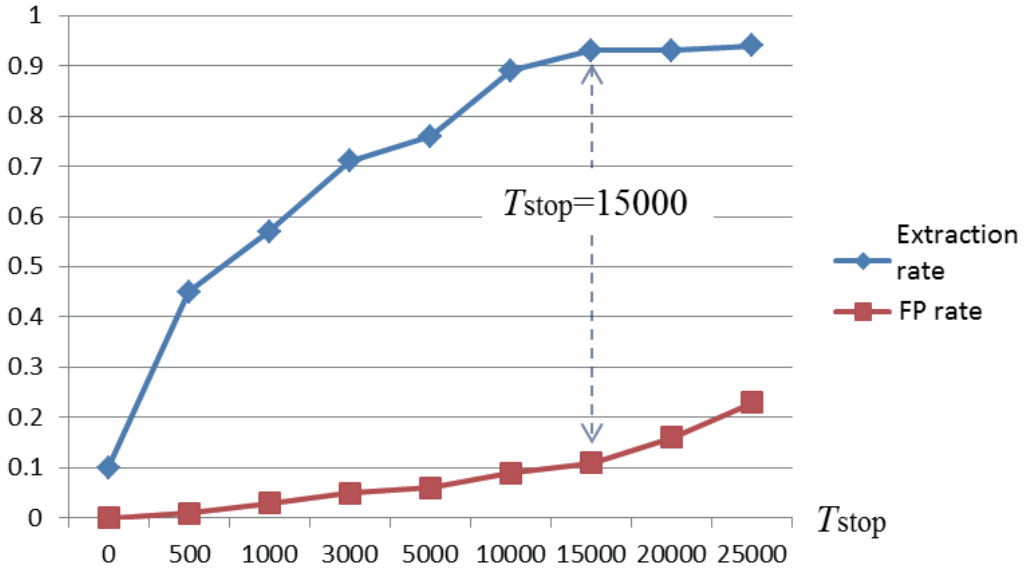

Figure 3.14: Illustration of the change sensitivity of segmented pulmonary blood vessels with the different settings of T_{stop}. When setting the T_{stop} to 15,000, we obtained most sensible results.

and the candidates of SPNs are shown in green. With the growing of T_{stop}, the regions of the blood vessel are propagated as well as the FPs of SPNs are reduced (Fig. 3.13).

We set the T_{stop} based on the sensitivity of segmented blood vessels. Since the extraction rate of segmented blood vessel grows few whereas the FP rate grows rapidly, while setting the T_{stop} larger than 15000 (Fig. 3.14), we set T_{stop}=15000 in the experiments. Table 3.2 shows the evaluation results of the pulmonary blood vessels segmented on ten CT images by setting the T_{stop} to 15000. The proposed method was able to extract blood vessel regions at 93%. Figure 3.13(e) shows an example of segmentation results. These results confirmed that the proposed method can segment blood vessels and nodules finely and separately.

3.4.2 Validation of pulmonary nodule segmentation

The performance of the proposed method on the segmentation of nodules was evaluated by using both dataset 1 and dataset 2. The evaluation results are given as detection

Table 3.3: TP rate and number of FPs on 20 standard-dose CT images using our proposed nodule detection method

Case	1	2	3	4	5	6	7	8	9	10	Avg.
Num. of nodules	15	19	19	22	23	22	33	61	83	107	40.4
Num. of FPs before fine segmentation	304	368	283	310	315	320	325	354	375	390	334
TP rate (%)	93.3	100	94.7	100	100	95.4	84.8	91.8	84.3	82.2	92.7
Num. of FPs after fine segmentation	7	8	11	9	11	6	8	10	12	15	9.7

Case	11	12	13	14	15	16	17	18	19	20	Avg.
Num. of nodules	2	2	2	2	2	4	3	4	3	2	2.6
Num. of FPs before fine segmentation	320	287	295	354	263	278	324	282	298	315	302
TP rate (%)	100	100	100	100	100	100	100	75	100	100	97.5
Num. of FPs after fine segmentation	10	12	8	11	10	7	9	12	9	11	9.9

rate (TP rate) and the number of FPs. Since a different setting of parameter ρ (in the neighborhood profile checking procedure of nodule checking processing) brings different detection results, we changed ρ from 0 to 0.8 with intervals of 0.1 to investigate the sensitivity of the proposed method by using standard-dose CT images. The FROC curve is shown in Fig. 3.15. When ρ was set to zero, we obtained the least number of FPs by 5.1/case, because almost all of the nodule candidates that were input into the neighborhood profile checking procedure were considered non-nodules. However, the detection rate was very low (72%), because all of the actual nodules connected to the blood vessels were incorrectly considered non-nodules. Both the detection rate and the number of FPs increased to accompany the growth of ρ. From the FROC curve shown in Fig. 3.15, the best results were obtained when $\rho = 0.3$. In this case, we obtained

Table 3.4: TP rate and number of FPs on 20 low-dose CT images using proposed nodule detection method

Case	1	2	3	4	5	6	7	8	9	10	Avg.
Num. of nodules	5	1	6	2	1	1	1	4	1	1	2.3
Num. of FPs before fine segmentation	226	336	238	293	407	371	339	348	406	493	346
TP rate (%)	100	100	83.3	100	100	100	100	75	0	100	85.8
Num. of FPs after fine segmentation	7	3	12	13	11	15	14	12	6	10	10.3

Case	11	12	13	14	15	16	17	18	19	20	Avg.
Num. of nodules	1	2	2	5	11	2	2	2	2	3	3.2
Num. of FPs before fine segmentation	278	228	311	467	128	235	407	276	244	390	296
TP rate (%)	100	100	100	80	90.1	100	100	75	100	100	97.1
Num. of FPs after fine segmentation	5	9	12	6	14	18	9	8	15	11	10.7

a 95% average TP rate with approximately 9.8 FPs/case. We also tested the proposed method by using dataset 2, with the same setting of parameter ρ. The results show that proposed method can extract about 91.5% nodules with 10.5 FPs/case from the low-dose CT images. The details of these results are shown in Table 3.3 and Table 3.4.

Figure 3.16 shows examples of nodules that are connected to the blood vessels. The proposed method can recognize such nodules separated from blood vessels and segment them (Fig. 3.16(c)). Among the 40 experimental CT images, the one with the largest number of nodules includes 107 nodules, and the least includes two nodules. The diameters of most nodules range from 3.0 and 5.0 mm; only 71 nodules are larger than 10 mm. Among the 471 nodules, the number of blood vessel-attached nodules is 131, the others are isolated nodules and pleura-attached nodules. The results in Table

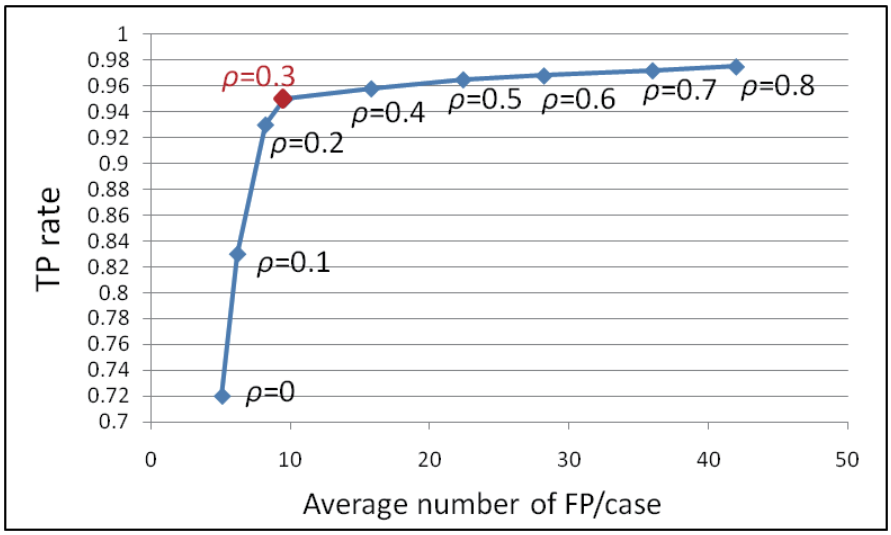

Figure 3.15: FROC curve for nodule detection with parameter of ρ.

Table 3.5: Comparison of proposed method to conventional methods

	Pulmonary blood vessels	Nodules	
Method	Extraction rate	TP rate	Num. of FP
OSF+FSP (Proposed)	93.0	95.1	9.8
GKC+FSP	91.6	95.2	16.2
LSE+RG	65.6	-	-
BSE+RSCC	-	95.2	46.8

3.3 and Table 3.4 show that the performance of the proposed method is stable, and confirm that our method is feasible for nodule segmentation from both standard-dose and low-dose CT images. By observing the segmentation results, we found that all of the 65 larger nodules, the isolated nodules were correctly segmented. Only one pleura-attached nodule in No. 9 case of low-dose CT image was miss-segmented, since this nodule was excluded from our extracted lung region.

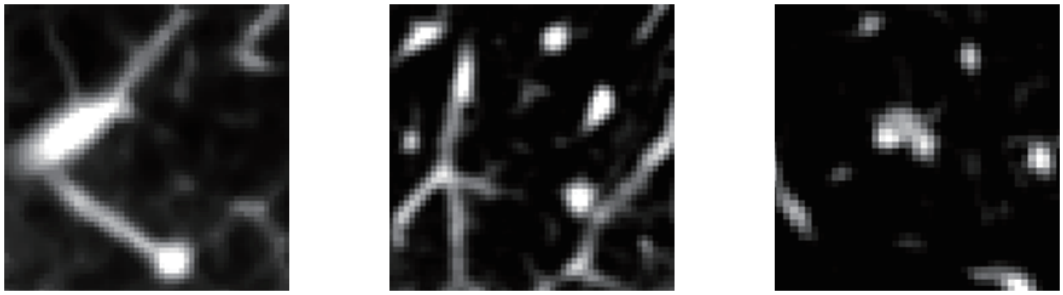

(a) Original image

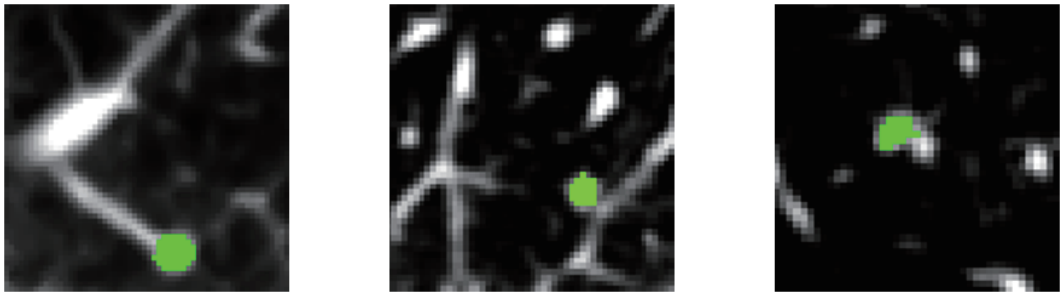

(b) Ground truth of nodules

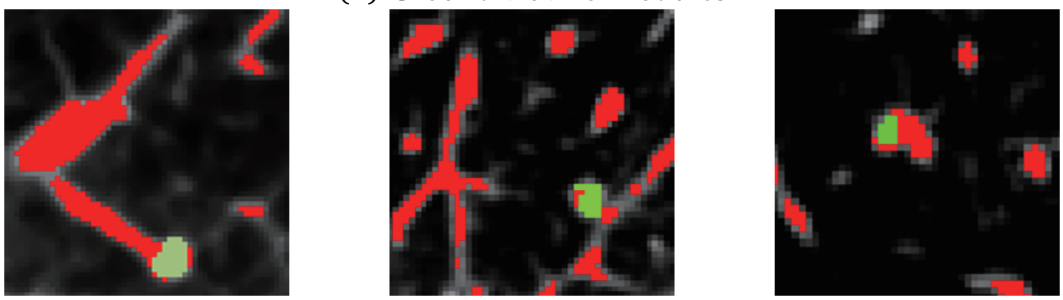

(c) Segmentation results

Figure 3.16: Examples of segmentation results of nodules connected to blood vessels. (a) shows original CT images, (b) shows true nodule regions painted in green. (c) shows segmentation results. Segmented nodules are shown in green; blood vessel regions are shown in red.

3.4.3 Comparison with conventional methods

Table 3.5 summarizes the comparison results of the proposed and conventional methods by using the stadndard-CT images obtained from dataset 1. The proposed method employed the OSF procedure for intensity structure analysis that was utilized to enhance the blood vessels and the nodules as the initial segmentation results. The conventional method for the intensity structure analysis was based on GKC. To compare the performance of OSF with GKC, we also applied a segmentation method consisting of GKC and

FSP on the same data set. The results in Table 3.5 show that the GKC+FSP method segmented blood vessel regions at 91.6%, which is similar to the proposed method. However, GKS+FSP method detected about 95% nodules correctly with 16.2 FPs/case, which produced 65.3% more FPs than the proposed method.

The proposed method incorporated the MS_LSE and MS_BSE filters to improve the segmentation performance of both the blood vessels and the nodules. The conventional segmentation methods of blood vessels or nodules usually only employs MS_LSE or MS_BSE filters to segment blood vessels or nodules. To verify the effectiveness of the proposed method that uses both filters, we also tested a pulmonary blood vessel segmentation method (LSE+RG) and a nodule detection method (BSE+RSCC) for several cases. Table 3.5 shows that the best performance was achieved by the proposed method.

3.5 Discussion

This paper proposed and evaluated an automatic segmentation method for both pulmonary blood vessels and nodules. We utilized the MS_LSE and MS_BSE filters to enhance line-like and blob-like structures as the initial blood vessels and nodules, respectively. In the local intensity analysis of the enhancement filter, the OSF procedure was utilized instead of the GKC procedure, because the GKC procedure usually causes undesired enhancement due to the smoothing process. The results of these initial segmentations were incorporated in fine segmentation, which significantly improved the segmentation performance of both the blood vessels and the nodules.

From the results in Tables 3.2, 3.3, 3.4 and 3.5, we confirmed that the proposed method is feasible for the segmentation of pulmonary blood vessels and nodules.

3.5.1 Effectiveness of optimum surface fitting

As mentioned in Section 3.2.3, we employed OSF instead of GKC for local intensity structure analysis to avoid the incorrect enhancement caused by smoothing. The com-

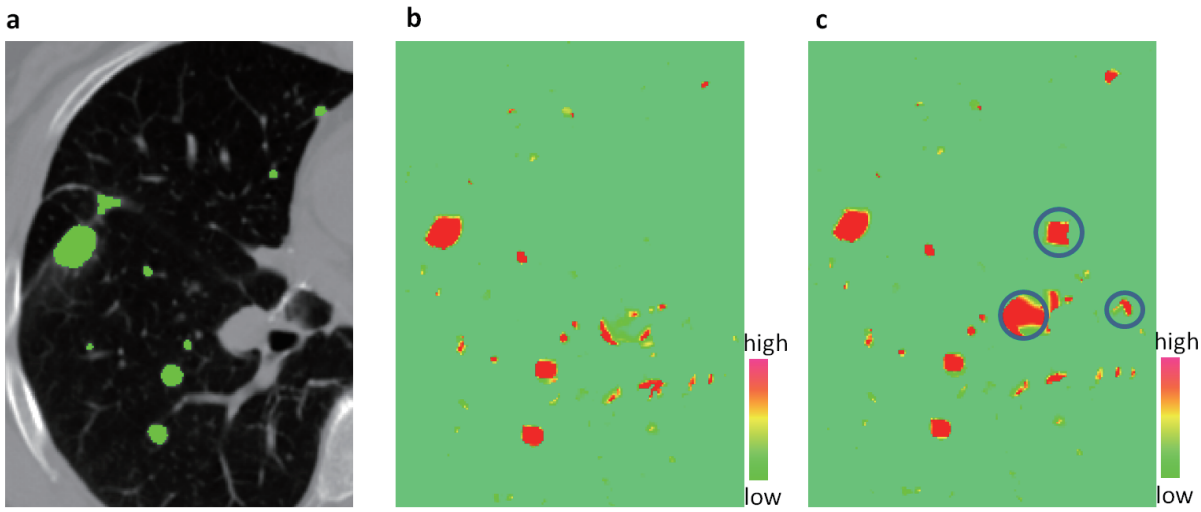

Figure 3.17: Comparison of BSE filter based on Gaussian kernel and surface fitting. (a) shows a chest CT slice with nodules painted in green. (b) shows the enhancement result of BSE filter based on surface fitting, and (c) shows the result of BSE filter based on a Gaussian kernel. Regions inside blue circles show incorrect enhancement at blood vessel regions

parison results of OSF and GKC-based methods show that the OSF-based method has better nodule detection performance. The reason is that Gaussian smoothing usually changes the intensity distribution of some blood vessel regions (particularly the bifurcation and thick vessels) to be much more blob-likely. The MS_BSE filter enhances such regions incorrectly (Fig. 3.17), which leads to FPs of the nodules and the shortage of blood vessels. Such a shortage of blood vessels usually shows small spheres; since we evaluated the segmentation results of pulmonary blood vessels by the number of blood vessel branches, the evaluation results of the method that consists of GKC and FSP has no large difference from the proposed method (Table 3.5).

3.5.2 Effectiveness of fine segmentation for pulmonary blood vessel segmentation

As shown in Table 3.5, the proposed method achieved better results than the conventional methods on the segmentation of pulmonary blood vessels. The proposed method

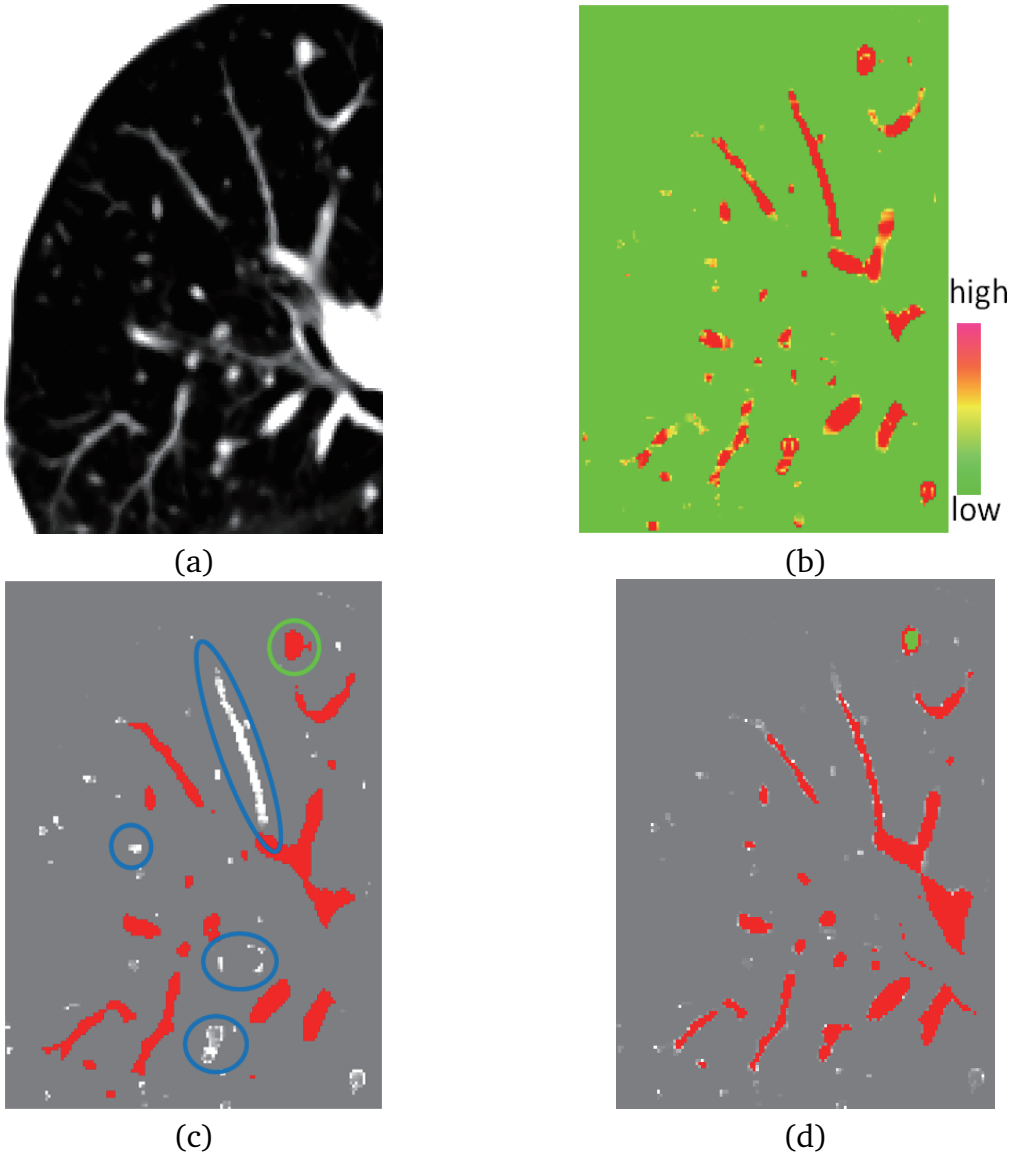

Figure 3.18: Illustration of blood vessel segmentation: (a) shows axial slice of input chest CT image, (b) shows the enhancement result of MS_LSE filter, (c) shows the segmentation result by region growing from initial blood vessels. Due to discontinuity, whole vessel tree cannot be segmented entirely (blue circles). Some nodules connected with vessels are incorrectly segmented (green circles). (d) shows the segmentation result of the proposed method.

utilized a new MS_LSE filter that has better performance for separating the vessel bifurcations and SPNs than the conventional one [111], especially while the largest eigenvalue λ_1 of Hessian matrix at the bifurcation point is close to 0. However, this new filter still has low sensitivity at several vessel bifurcations, which leads to the dis-

continuity of initial pulmonary blood vessels I_{lse} (Fig. 3.18(b)). The I_{lse} also includes several nodule regions because of the incorrect enhancement of the MS_LSE filter (Fig. 3.18(b)). Thus, if perform the LSE+RG method on I_{lse} to address the fine segmentation of blood vessels, segmenting the whole vessel tree is difficult, and the nodules that are connected with blood vessels will be segmented incorrectly (Fig. 3.18(c)). The results shown in Table 3.5 also indicate that the LSE+RG method was insufficient for the segmentation of pulmonary blood vessels. We improve the segmentation performance by incorporating initial pulmonary blood vessels I_{lse} and nodule candidates I_{bse}, a speed function that performs fast propagation at I_{lse}, and performs slow propagation at I_{bse} to propagate the front surface. Consequently, the nodules connected to the blood vessels were suppressed in the proposed fine segmentation of blood vessel (Fig. 3.18(d)). Fig. 3.18(d) also shows that our FSP scheme can avoid the discontinuity of blood vessels and segment the whole pulmonary blood vessel tree. The reason is that at the discontinuity points of initial blood vessels I_{lse}, although the speed of surface propagation becomes slower, the front surface will still be propagated to cover such regions unless it belongs to the nodule candidates in I_{bse} or the function F_{margin} (Eq.(3.16)) outputs a small value.

3.5.3 Effectiveness of fine segmentation for pulmonary nodule detection

The results in Tables 3.3, 3.4 and 3.5 show that the fine segmentation procedure has good performance for FP reduction. The nodule candidates that were obtained by MS_BSE filter included around 300 FPs/cases (Tables 3.3, 3.4). After fine segmentation, the number of FPs was reduced significantly. This also proved that the FPs were mostly produced in the blood vessel regions. When the TP rate is around 95%, the number of FPs of the BSE+RSCC method is 46.8/cases, which is insufficient as a nodule detection method. Augmentation of the threshold in RSCC may lead to fewer FPs, but usually the TP rate will also be significantly reduced.

The common approach reducing FPs for nodule detection is to classify nodules and

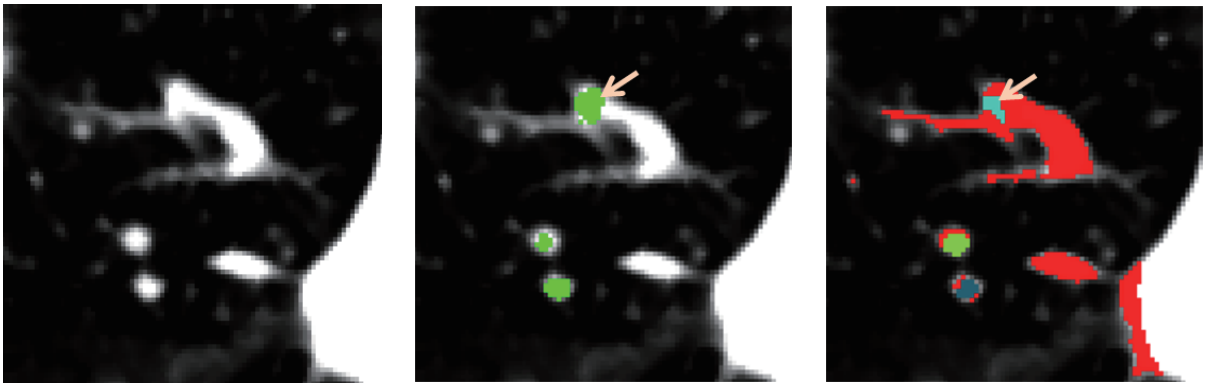

(a) (b) (c)

Figure 3.19: Illustration of nodule segmentation: (a) shows axial slice of input chest CT image, (b) shows nodule candidates obtained by MS_LSE filter. The FP indicated by the arrow shows a regular sphere region. (c) shows a front surface terminating at the FP and indicates an irregular shape.

FPs by utilizing several geometric features [[74, 86, 120]]. However, the FPs included in the nodule candidates often show regular spherical shapes as well as the actual nodules (Fig. 3.19(b)), which complicates classification. As mentioned earlier in Section 3.2.4.4, in our FSP procedure, the front surface that terminats at such FPs shows irregular shape (Fig. 3.19(c)), and the neighborhood profile of such FPs differs from that of an actual nodule. By investigating these two profiles, we executed a *nodule_ checking procedure* during fine segmentation, which can help classify the actual nodules and FPs and achieve gratifying results. In addition, only the nodule candidates that are connected to the blood vessels will be input into the *nodule_ checking procedure*, which guarantees that all the isolated nodules and pleura-attached nodules will be segmented correctly.

3.5.4 Limitations

Although the proposed segmentation method in this chapter provided good performance in the segmentation of both lung nodules and blood vessels, this method still has some limitations as follows:

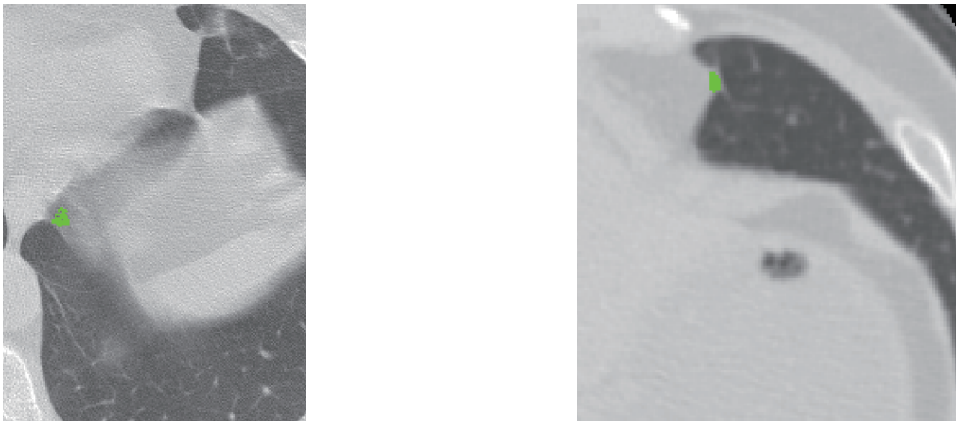

(a) (b)

Figure 3.20: Examples of FPs that occurred in the mediastinum region. The region marked by green shows two examples of the FPs.

(1) The performance of nodule detection depends on the pulmonary vessel segmentation results, and vice versa. The proposed method aims to improve the segmentation performance of both SPNs and vessels by incorporating the information of their initial segmentation results into the fine segmentation. A FSP procedure executed the fine segmentation that can segment SPNs and blood vessels by separating them. However, if the segmentation of blood vessels fails, the accuracy of nodule segmentation will worsen.

(2) The proposed method cannot reduce the FPs that are generated in other organs such as bones, chest walls or cardiac area. The proposed method focuses on discriminating the nodules and blood vessels to improve segmentation performance. Most FP that occurs at blood vessel regions can be removed. However, several FPs may occur in bone, chest wall and mediastinum region (Fig. 3.20). The proposed method cannot reduce such FPs.

(3) Several incorrect discriminations between nodules and vessels still occurred. The proposed method failed to reduce several FPs in vessel bifurcations that were strongly enhanced by the BSE filter.

3.6 Conclusion

This chapter presented a novel segmentation method of pulmonary blood vessels and nodules. The initial segmentation results were obtained by enhancement filters that are based on local intensity analysis. Then we combined the initial segmentation results of the blood vessels and nodules into an FSP procedure to perform fine segmentation, which can improve the segmentation results significantly. The experimental results showed that the proposed method can simultaneously segment both the pulmonary blood vessels and the nodules finely. Also, the experimental results proved that the performance of the proposed method is better than the compared conventional methods, which confirmed the effectiveness of this method. Future work includes (a) the reduction of FPs at non-vessel regions of the nodule detection method, (b) evaluation through a large number of cases, and (c) the application of the proposed method to actual CAD systems.